Master Thesis

Source Analysis of the Auditory Steady State Response for varying Modulation Frequencies: A combined EEG-MEG Group Study

Yvonne Buschermöhle

March 2021

Westfälische Wilhelms-Universität Münster

supervised by

PD Dr. Svetlana Gurevich
Institut für Theoretische Physik

Prof. Dr. Carsten Wolters
Institut für Biomagnetismus und Biosignalanalyse

Acknowledgements

Several people have contributed to the successful completion of this Master thesis. I therefore express my gratitude to

- Prof. Dr. Carsten Wolters, PD Dr. Svetlana Gurevich and Dr. Oliver Kamps for enabling and supervising this Master thesis.
- Andreas Wollbrink for technical support and enriching methodological input.
- Karin Wilken, Ute Trompeter and Hildegard Deitermann for helping me acquire subjects and conducting the measurements, even during the Covid-19 pandemic.
- my family, who has supported me in all possible ways during my years of studies.

Abstract

The study investigates the influence of the modulation frequency (MF) on the strength of the Auditory Steady State Response (ASSR) in a combined EEG-MEG measurement. It is hypothesized, that the asymmetry of the hemispheres in the processing of the ASSR leads to different shapes of the ASSR profile and possibly to different resonance frequencies of the left and right auditory cortices. Further, the influence of the baseline correction method on the resonance frequency is investigated.

MEG and EEG was acquired from 8 subjects (50% female, $M_{\text{age}} = 25.5$, $SD_{\text{age}} = 2.7$), who perceived sinusodial sounds on both ears, which were amplitude modulated with different modulation frequencies ranging from 16 Hz to 61 Hz. ASSR profiles were obtained by an analysis of the central electrode signals and by a source analysis of the MEG data, using a BEM head model and dSPM source reconstruction. All analyses were conducted in the frequency domain in order to avoid time averaging.

It was shown, that the resonance frequency differs between the left and right auditory cortices for most subjects and neither of the hemispheres dominates the ASSR profile obtained by the central electrode analysis. The resonance frequency is further influenced by the choice of the baseline correction method (absolute or relative). At least two different types of ASSR profile shapes were found.

Possible reasons for the unsufficiency of the EEG lie in the different lateralization for varying modulation frequencies and possibly in different source orientations. The necessity of an individual transcranial alternating current stimulation (tACS) of the hemispheres is implied, if the stimulation is based on the resonance frequency. Further investigation on the asymmetry of the hemispheres and the meaning for tACS is suggested.

Contents

1 Introduction

The discovery of the auditory steady state response (ASSR) has enriched the neuroscientific research community with a concept, which permits many different scopes of application. According to the state of research, it can for example be used to determine hearing loss [24] and abnormalities in the ASSR are investigated as a potential biomarker for psychiatric disorders such as schizophrenia (for an overview, see [43]). Many studies have shown that the strength of the ASSR depends on different parameters, such as attention [13, 35], volume of stimulus presentation [33], carrier frequency [27] but also on the modulation frequency [2, 16, 33].
An important application has been shown by Baltus [3]: if the auditory cortex is stimulated with a transcranial alternating current (tACS) of a frequency slightly exceeding the modulation frequency, which elicits the strongest ASSR (called resonance frequency), an improvement in the ability to detect gaps between sounds is observed [3]. In order to optimize the effect of the tACS, the determination of the correct resonance frequency is crucial and shall be the topic of this thesis. In many applications the resonance frequency is determined by the activity measured in one or few EEG electrodes [2, 3, 49]. However, it has been established, that the measurement of the ASSR is well performed with MEG data due to the tangential orientation of the sources (see e.g. [23,33,40]). Therefore, this study evaluates the dependence of the ASSR on the modulation frequency in a combined EEG and MEG measurement. This procedure offers the possibility to execute and compare different analysis methods.

First of all, a comparison between the determined resonance frequencies via EEG and MEG will be performed. So far, only one study is known to have measured the ASSR in both EEG and MEG, conducting two separate measurements, where a high test-retest-reliability was found in both modalities [26]. Nevertheless, no variation of the modulation frequency has taken place in this study and therefore still needs investigation. The EEG-sensor analysis can be considered the most cost efficient and easiest way to measure and analyze the ASSR and it shall be compared with the source analysis of the MEG-data, using a realistic headmodel. The latter process is more expensive, both financially and computationally, however, it is expected to bring the cleanest and most detailed results.

The second analysis deals with the asymmetry between the left and the right hemisphere, when it comes to the processing of the ASSR. While the N1 component of the Auditory Evoked Potential/Field is found to be dominant contralateral to the stimulated ear [34], previous studies have shown, that the right hemisphere shows a dominant actvity compared to the left one, when evoking the ASSR [31, 34, 40]. A study conducted by Poelmans et al. [31] has shown that the hemispheres act very differently when processing the ASSR. The strength of the response in each hemisphere depends on the stimulation (ipsilateral, contralateral or bilateral) and the modulation frequency. Furthermore, a decreased ASSR in the left hemisphere was found in subjects suffering from dyslexia. This asymmetry has led the author to the assumption, that the resonance frequency of the hemispheres might aswell

differ. Therefore, a detailed analysis of the ASSR profile in the individual hemispheres for bilateral stimulation is performed in this study.

Subsequently, a third parameter shall be investigated, namely the type of baseline correction. In order to avoid the effect of signal cancelling by averaging phase-instable oscillations in the time domain, the analysis will be fully completed in the frequency domain. In cerebral power spectra, a 1/f behaviour can be observed, which so far has no theoretical explanation. In order to compare the peaks of different modulation frequencies, this behaviour has to be corrected for. Different possibilities of baseline correction methods are established in the research community. Since the correction methods show different preferences for higher or lower frequencies, it is believed that the choice of the baseline correction method influences the resulting resonance frequency in a subject. Therefore, two different methods will be used and compared.

Finally a methodological aim of this study is to explore the analysis options offered by the Matlab-based toolbox Brainstorm [39]. Hence, all analysis steps will be performed with the tools offered by Brainstorm or own scripts based on Matlab codes.

A group study of 8 healthy participants will be conducted. This sample size permits the analysis on an individual level, while simultaneously having a small pool of subjects, which might (and will) show different behaviours on the investigated matters.

2 Theoretical Foundations

All important theoretical foundations shall be explained in this chapter. Starting from the physiological explanations of the EEG- and MEG-signals it will lead to a mathematical overview about how to localize and analyze the cerebral sources.

2.1 Physiological Foundations

The focus of this study is the cerebral cortex, which is the uppermost layer of the brain and has a complexly folded surface area. It is divided into two hemispheres (left and right), which in turn consist of four lobes (temporal, frontal, parietal and occipital) [20]. Different regions of the cortex can be assigned specific functions, such as seeing (visual cortex) or hearing (auditory cortex), as roughly presented in figure 2.1. The brain mainly consists of glia cells and neurons. The former are important for structural support and the transportation of nutrients, while the latter are responsible for the processing of information. Neurons consist of the soma (cell body), containing the nucleus, as well as two types of extensions: the dendrites, which perceive signals from other nerval cells, and the axon, which forwards signals to other neurons. Pyramidal and stellate cells can be considered as the two main groups of cortical neurons, with the former being relatively large and their dendrites perpendicular to the cortical surface. The inside of the neuronal cell has a potential difference of $-60\,\mathrm{mV}$ to $-80\,\mathrm{mV}$ to the outside, which is called the resting potential. It arises due to a concentration gradient of the K^+, Na^+ and Cl^- ions, which is kept constant by the sodium-potassium-pump, enabling the ions to diffuse through the membrane [1] [8]. When a neuron is activated, additional voltage-gated ion channels open up and more Na^+ ions can pass through the membrane into the cell. As they do, the intracellular potential gets less negative (depolarization), leading to the opening of even more ion channels. If the potential is increased to a critical value of about $-55\,\mathrm{mV}$ or more[2], a very rapid change of the membrane's potential can be observed, which is referred to as the action potential. According to the all-or-nothing property, the action potential shows the same amplitude every time it is released. Stronger stimuli result in more frequent action potentials. The signal, which emerges at the axon hillock, moves along the axon. When it reaches a synapse (the

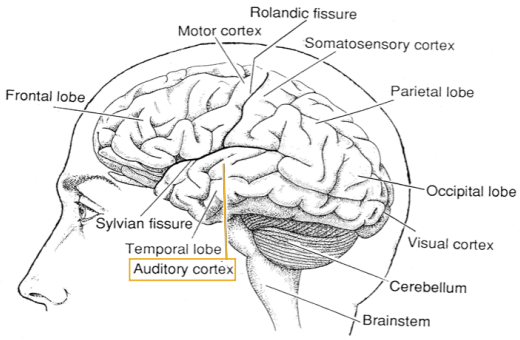

Figure 2.1 The human brain including indication of specific areas in the cerebral cortex *(taken from [20], auditory cortex highlighted by author).*

[1] For a detailed description see [8], pp. 1414-1425.
[2] Different threshold values can be found in the literature, see for example [8], [20].

junction between two nerval cells), neurotransmitters open membrane channels of the connected neuron. Therefore, this so-called postsynaptic neuron is depolarized or hyperpolarized, leading to an exciting or inhibiting postsynaptic potential (PSP) respectively. PSPs can add up temporally or spatially (synchronization of PSPs from different synapses); exciting and inhibiting PSPs can counteract each other. The resulting PSP leads to a new action potential in the postsynaptic cell, if the threshold is passed. The synaptic currents perform on a slower time scale than the action potential and therefore create the largest part of the measured EEG and MEG signals. The resulting activity can be thought of as primary current dipoles, which are represented by large arrows in figure 2.2 and volume currents in the surrounding medium, which are illustrated by the dashed lines in the upper figure. While the primary currents are caused by the movements of ions due to the above mentioned processes, the volume currents complete the flow of ions in order to prevent the buildup of charge [20]. The lower figures schematically show the magnetic field and the electric potential, which are caused by the source. The activity can be described with the Maxwell equations (see section 2.5.1).

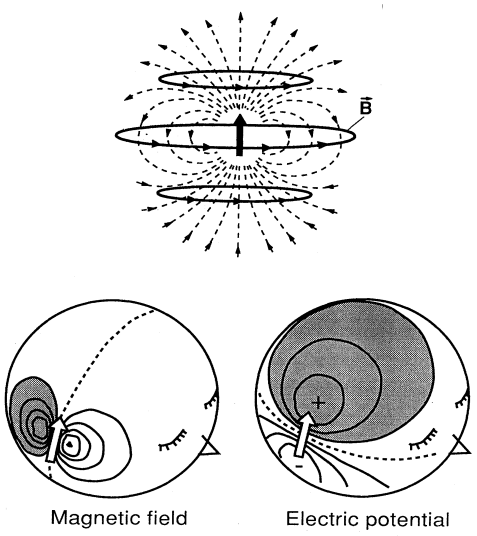

Figure 2.2 Emerging electro-magnetic field of a current dipole (upper) and schematic illustration of the field patterns on the scalp (lower) [20].

2.2 EEG and MEG Signals

As explained in section 2.1, the electric sources resulting from brain activity have a dipolar form, creating a corresponding electromagnetic field. Both, the electric and the magnetic components of the emerging electromagnetic field can be measured non-invasively on the scalp via Electroencephalography (EEG) or Magnetoencephalography (MEG) respectively. Since the two fields are perpendicular to each other, EEG and MEG are complementary rather than competing methods: both have strengths as well as weaknesses and depending on the question being addressed, the one, the other, or a combination of the modalities is required.

First discovered in 1924 by Hans Berger [6], the method of EEG has been continuously improved and is one of the most commonly used methods to measure cerebral activity. Its low costs and uncomplicated utilization has brought population in a great variety of neuroscientific and medical applications. Several electrodes are placed on the scalp, from which one serves as a reference. Position and amount of the electrodes can be adjusted depending on the

application. The temporally fluctuating potential difference between each electrode and the reference is then measured with a certain sampling frequency. Since the signal is rather small, it needs to be amplified. [42]

Analogously, the magnetic field can be measured, but it requires some more technical effort. Therefore it is a relatively new method compared to EEG and has only been used since 1968, when it was discovered by David Cohen [9]. Since the emerging magnetic signals ($\sim 10^{-15}$ T to 10^{-11} T) are much weaker than the earth's geomagnetic field ($\sim 10^{-6}$ T), the measurements have to be conducted in a magnetically shielded room. Other than in EEG, the subjects sit under a permanently installed helmet, which contains the sensors. State-of-the-art MEG devices contain more than 300 sensors, which cover the entire head. At each sensor, the signal is detected by a pickup coil in the form of an axial gradiometer[3], producing a current proportional to the signal's strength. At the input coil, it is then coupled to the Superconducting Quantum Interference Device (SQUID). SQUIDs are able to measure magnetic fields of extremely small amplitudes, such as in this context. It consists of a superconducting loop, interrupted by two Joseph junctions and kept at a low temperature by liquid helium (for details see [20]).

It is possible to combine the two modalities by wearing the EEG-cap while sitting in the MEG device. This permits to measure the emerging electric and the magnetic fields simultaneously and therefore obtaining a maximal amount of information on the activity. EEG and MEG data both show a high temporal, and a moderate spatial resolution. It is therefore necessary to complement the dataset with image data of the head, which is typically obtained by Magnetic Resonance Imaging (see section 2.3 for a short description).

The resulting data are amplitudes recorded over time, measured in Volt or Tesla respectively. By repeating a certain stimulus and averaging recorded epochs with the stimulus onset at the same relative timepoint, a so-called evoked response can be computed. Since oscillations caused by noise are not causally related to the stimulus onset, they are cancelled by the averaging process. In contrast, the signal is highly correlated to the stimulus onset and is therefore not affected by the averaging process, resulting in a response with a certain signal to noise ratio (see section 2.4 for a brief example).

For some analyses however, it is useful to transfer the data from the time into the frequency domain, especially when oscillations with specific frequenices are of interest. This can be accomplished with a discrete Fast Fourier Transform. Due to the finiteness of the temporal data, the resulting periodogram has a resolution of $\frac{1}{T}$ and contains noise. In order to reduce this noise, it is common to use Welch's Power Spectrum [47] as a measure of the frequency power. By applying it, the data is segmented into time windows (overlapping or not) of the same size L. The FFT is then applied to each window and the computed spectra are averaged (for a detailed description see [47]). Using Welch's Power Spectrum instead of the FFT leads

[3]Other pickup coils are possible, see e.g. [22]

to a smoother Power Spectrum, but it will also show a lower resolution, which is reduced to $\frac{1}{L}$.

The typical Power Spectrum of background brain activity roughly has a shape of $\frac{1}{f}$ with potential peaks at certain frequencies for specific brain activities, or noise (e.g. line noise). In figure 2.3 an examplary Power Spectrum of MEG or EEG data with strong activity in the alpha band (7 Hz to 14 Hz) is shown. However, the $\frac{1}{f}$-shape is only an approximation and no explanation for this shape can be deduced from theory. Hence, the background needs to be corrected for, when comparing the activity peaks at different frequencies. Several methods for this correction are available. Most recently, an approach by Donoghue et al. [14] has gained popularity, suggesting an elaborate method to detect peaks in the EEG or MEG Power Spectrum without recording an additional baseline data set. However, the proposed approximation of a Gaussian for the peak, is inappropriate for the data recorded in this study, since the activity will be highly frequency specific and hence the peak too narrow. Therefore, the recording of baseline data and signal data will be necessary. In this thesis, the absolute and the relative change of the spectrum between baseline and signal measurement are used and compared. For further details, see section 4.1.

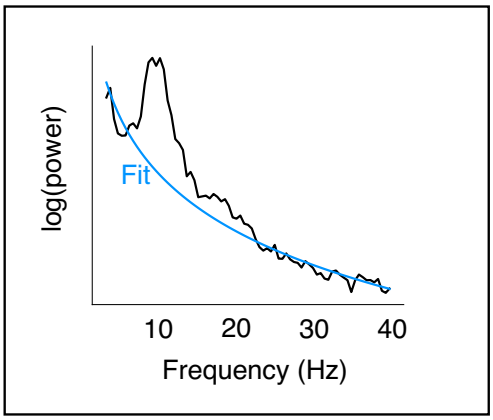

Figure 2.3 Typical Power Spectrum of data recorded by MEG or EEG including a peak at the alpha activity and a fit of $\frac{1}{f}$ for visualization [14].

2.3 Magnetic Resonance Imaging (MRI)

The core of this study is EEG and MEG data, but additional information is needed, which links the functional data to the head geometry. A common and radiation-free method to extract the physiological geometry is Magnetic Resonance Imaging (MRI). In MRI measurements, subjects are exposed to a strong external magnetic field (in z-direction). The hydrogen nuclei in the body, consisting of only a proton with a magnetic moment, try to align with the external magnetic field lines, but due to the conservation of the angular momentum never reach the fully aligned position. Instead, they precess around the field lines in an (almost) parallel or anti-parallel state at the Larmorfrequency. A small excess of parallel-oriented protons leads to a net mangetization in parallel direction. With an additional high-frequency magnetic field, which is orthogonal to the static magnetic field, the protons are synchronized and the total magnetization precesses in the x-y-plane. When switching off the temporary magnetic field, the realignment along the static magnetic field requires a different amount of time for the protons, depending on the surrounding tissue. This leads to a dephasing of the

protons. The so-called relaxation time, which is required to reach 63% of the original longitudinal magnetization, is denoted by T1 and determines the contrast in the resulting images. These images show slices of (in this case) the human head. Since the tissues in the brain have different amounts of protons, the image permits to differentiate them by the contrast. In T1-weighted images, as they will be used in this study, fluids (such as liquor or blood) are dark. Tissues containing less water (and therefore less hydrogen atoms) are bright. For a short introduction to MRI see [44], for a more detailed description see for example [46].

2.4 Auditory Steady State Response

When perceiving a sound, the human brain responds with a so called Auditory Evoked Potential (AEP) in EEG or an Auditory Evoked Field (AEF) in MEG, respectively. Figure 2.4 shows an examplary AEP including its components[4], which has been evoked by a click sound. The Auditory Steady State Response (ASSR) describes the AEP/AEF which is evoked by a repeated sound, such as recurring click sounds, frequency or amplitude modulated sinusoidals (see fig. 2.5). It has first been discovered by Robert Galambos et al. in 1981 as the "40 Hz auditory potential" [16]. In an experiment the researchers found that the brain potential (measured via EEG electrodes) for click tones peaked when presented with a frequency of 40 Hz. Although historically, the ASSR refers to this 40 Hz signal (e.g. amplitude modulated sinusoidal tones with a 40 Hz modulation frequency), it can also be evoked by other modulation frequencies and the oscillation of the steady state response is then determined by this frequency.

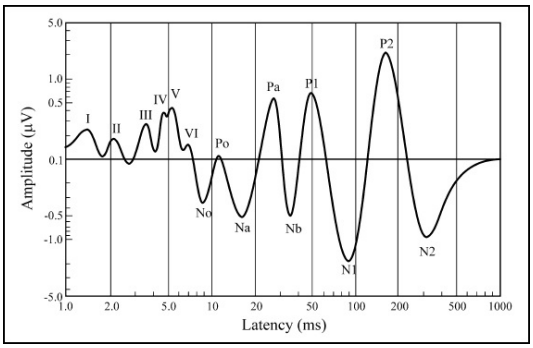

Figure 2.4 Auditory Evoked Potential at the electrode Cz as response to a click sound presented [28].

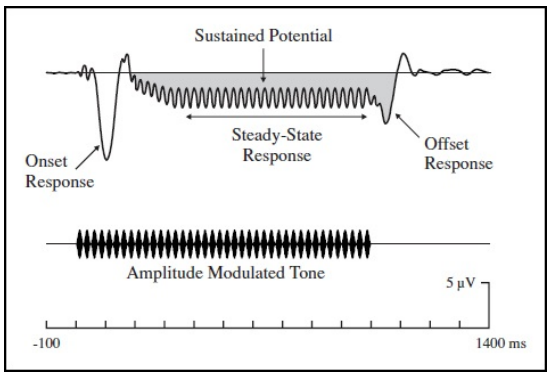

Figure 2.5 Auditory Evoked Potential as a reaction to an amplitude modulated tone lasting for 1s. Transient on- and offsets such as the Steady State Response are marked, the ASSR is shaded in grey [28].

It is a widespread concept to measure the ASSR with either EEG or MEG sensors and analyze the data on a sensor level (as in [3, 49]) and/or on a source level (as in [32, 33, 40]). Only one study so far has been found to combine the modalities and separately measure EEG and

[4]For a detailed description of the components, see ch. 1 in [28].

MEG [26] in order to determine a reliability of the 40 Hz ASSR measurements, which has found to be high.

In terms of the Power Spectrum, the aperiodic background signal (cf. section 2.2) is observed with additional narrow peaks at the modulation frequency and possibly at the harmonics [33]. The modulation frequency, which evokes the strongest signal, is referred to as the Resonance Frequency [5] which can vary between subjects [3, 33]. The shape of the curve showing the ASSR-strength as a function of the modulation frequency (ASSR profile) found in Ross et al. [33] is shown in the uppermost curve in figure 2.6. It shows the grand average of the ASSR profiles in the left hemisphere over 8 subjects, measured with MEG. A peak of the ASSR is found at 40 Hz and a smaller peak is found around 20 Hz. A similar profile was found in Baltus et al. [2] with EEG electrodes. However, subjects with different shapes of the resulting profile were excluded from the study and it is therefore not representative for all subjects.

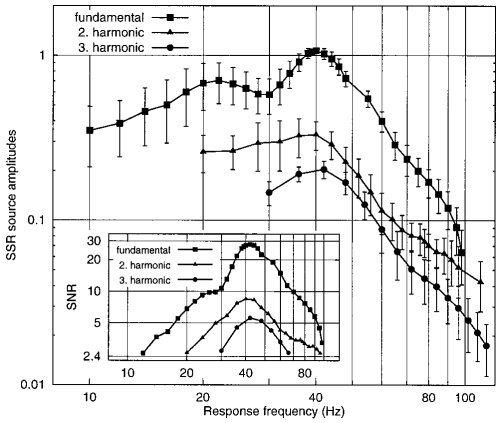

Figure 2.6 Grand average of the ASSR profile for 8 subjects [33].

According to Pantev [27], the ASSR can be localized in the auditory cortex, slightly more medially and anteriorly than the sources found for the N1 response. A tonotopy in the processing can be observed for varying carrier frequencies. An asymmetry in the processing of the ASSR between the left and the right hemisphere has been found in several studies. While for example somatosensory evoked responses always appear in the contralateral hemisphere, the processing of the ASSR appears to be more complicated. For most studies, the right hemisphere has been found to be dominant [34, 40, 45], however at least one study suggests the contrary and finds the left hemisphere to dominate [48]. Poelsmann et al. [31] show, that the strength of the response in each hemisphere depends on the stimulated ear (ipsilateral, contralateral or bilateral), the type of stimulation (syllabic- or phonemic-rate modulations) and on the modulation frequency of the stimulus (4 Hz, 40 Hz or 80 Hz).

The underlying mechanism for the emergence of the ASSR is also a highly debated topic in the scientific community. When first discovered, the ASSR was considered a superimposition of repeated transient middle latency responses (MLR), which describes the evoked response from $\approx$ 10 ms to 50 ms after stimulus onset. The MLR peaks around 25 ms at component Pa (see fig. 2.4), what has led to the idea to repeat the stimulus in a periodic manner in the corresponding frequency of 40 Hz [16, 23, 29, 38, 41]. Other researchers claim, that the ASSR is more than the sum of the MLRs. In several studies it has been shown, that the

[5] In the literature, there is no consistent term for this phenomenon and it might also be referred to by different terms such as "preferred oscillation frequency" [49], "Individual Gamma Frequency" [3] or other.

superimposition of the MLRs leads to slight, but not neglectable differences compared to the measured ASSR [1, 4, 36]. Since the results of this thesis are independent from the reason of emergence, the matter shall not be further discussed.

The ASSR has a broad variety of applications in medical research: it can for example be used as a biomarker for schizophrenia [43], to determine hearing thresholds [24] and to investigate speech intelligibility and dyslexia [19]. Further, it has been shown, that a low resonance frequency correlates with a decreased ability to detect gaps between sounds [2].

2.5 Forward Problem in EEG and MEG

The overall aim of source analysis is to reconstruct the location and moment of cerebral activity from EEG and MEG data. The posed problem is not well defined and prior information are required to obtain a reasonable source estimation. Before being able to address this so-called inverse problem, it is necessary to solve the forward problem, where the magnetic and electric signals at the sensors are computed, in the case of a known cerebral source. The basic ideas of solving the forward problem are presented in the following sections. These computations are the foundation of solving the inverse problem, which will be presented in section 2.6.

2.5.1 Quasistatic Approximation

Dealing with electromagnetic fields, the fundamental equations are found in the Maxwell equations

$$\nabla \cdot \boldsymbol{E} = \frac{\rho}{\epsilon_0} \tag{2.1}$$

$$\nabla \times \boldsymbol{E} = -\partial_t \boldsymbol{B} \tag{2.2}$$

$$\nabla \cdot \boldsymbol{B} = 0 \tag{2.3}$$

$$\nabla \times \boldsymbol{B} = \mu_0(\boldsymbol{J} + \epsilon_0 \partial_t \boldsymbol{E}), \tag{2.4}$$

where $\boldsymbol{E}$ denotes the electric field, $\boldsymbol{B}$ the magnetic field, $\boldsymbol{J}$ the total current density and ∂_t the partial derivative with respect to time. Following the elaboration of Hämäläinen et al. [20], it will be shown that in the context of this work, the approximations $\partial_t \boldsymbol{E} = 0$ and $\partial_t \boldsymbol{B} = 0$ are justified, leading to a simplified version of the Maxwell equations.
The current $\boldsymbol{J}$ in a passive non-magnetic medium can be rewritten as a sum of the ohmic current and the polarization current

$$\boldsymbol{J} = \sigma \boldsymbol{E} + \partial_t \boldsymbol{P}, \tag{2.5}$$

where $\boldsymbol{P} = (\epsilon - \epsilon_0)\boldsymbol{E}$ is the polarization. Rewriting the electric field as

$$\boldsymbol{E} = \boldsymbol{E_0}(\boldsymbol{r}) e^{i2\pi f t}, \tag{2.6}$$

equation 2.4 yields

$$\begin{aligned}\nabla \times \boldsymbol{B} &= \mu_0[\sigma \boldsymbol{E} + \partial_t \boldsymbol{P} + \epsilon_0 \partial_t \boldsymbol{E}] \\ &= \mu_0[\sigma \boldsymbol{E} + \partial_t(\epsilon - \epsilon_0)\boldsymbol{E} + \epsilon_0 \partial_t \boldsymbol{E}] \\ &= \mu_0(\sigma \boldsymbol{E} + \epsilon \partial_t \boldsymbol{E}). \end{aligned} \tag{2.7}$$

In order to rightfully neglect the term $\partial_t \boldsymbol{E}$, condition 2.8 needs to be fulfilled.

$$\begin{aligned} &|\sigma \boldsymbol{E}| \gg |\epsilon \partial_t \boldsymbol{E}| \\ \overset{2.6}{\Leftrightarrow} &\frac{2\pi f \epsilon}{\sigma} \ll 1 \end{aligned} \tag{2.8}$$

The left hand side of the condition consists of parameters, that can be estimated. Hämäläinen suggests to choose

$$\begin{aligned} \sigma &= 0.3 \frac{1}{\Omega \mathrm{m}} \\ \epsilon &= 10^5 \epsilon_0 \\ f &= 100\,\mathrm{Hz}, \end{aligned}$$

which leads to $\frac{2\pi f \epsilon}{\sigma} = 2 \cdot 10^{-3}$, which indeed fulfills the required condition.
Further it has to be shown, that $\partial_t \boldsymbol{B} = 0$ is justified. For this purpose, the cross product of equation 2.2 is considered:

$$\begin{aligned}\nabla \times \nabla \times \boldsymbol{E} &= \nabla \times (-\partial_t \boldsymbol{B}) \\ &= -\partial_t (\nabla \times \boldsymbol{B}) \\ &= -i 2\pi f \mu_0 (\sigma + i 2\pi f \epsilon) \boldsymbol{E} \end{aligned} \tag{2.9}$$

which leads to the characteristic length scale

$$\lambda_c = \left| 2\pi f \mu_0 \sigma (1 + \frac{i 2\pi f \epsilon}{\sigma}) \right|^{-\frac{1}{2}} \approx 65\,\mathrm{m}. \tag{2.10}$$

Hence solutions of equation 2.9 show spatial changes on a length scale that is much larger than a human head's diameter and can therefore also be neglected. These approximations

lead to the quasi-static Maxwell equations

$$\nabla \cdot \boldsymbol{E} = \frac{\rho}{\epsilon_0} \tag{2.11}$$

$$\nabla \times \boldsymbol{E} = 0 \tag{2.12}$$

$$\nabla \cdot \boldsymbol{B} = 0 \tag{2.13}$$

$$\nabla \times \boldsymbol{B} = \mu_0 \boldsymbol{J} \tag{2.14}$$

and due to equation 2.12 it is possible to express the electric field as the negative gradient of a scalar potential:

$$\boldsymbol{E} = -\nabla V, \tag{2.15}$$

which will simplify the following computations.

2.5.2 Primary Current

The considered current density $\boldsymbol{J}$ can be divded into two parts, acting on different length scales: the volume current $\boldsymbol{J}^v = \sigma \boldsymbol{E}$, resulting from the macroscopic electric field on charge carriers in the conducting medium and the primary current $\boldsymbol{J}^p$, acting on a cellular level.

$$\boldsymbol{J}(\boldsymbol{r}) = \boldsymbol{J}^p(\boldsymbol{r}) + \sigma(\boldsymbol{r})\boldsymbol{E}(\boldsymbol{r}) \overset{2.15}{=} \boldsymbol{J}^p(\boldsymbol{r}) - \sigma(\boldsymbol{r})\nabla V(\boldsymbol{r}) \tag{2.16}$$

While the primary current is considered to be active, meaning the driving battery in a cell, the volume current flows passively in the medium. The primary current is ordinarily modeled as a current dipole $\boldsymbol{Q}$ at the location $\boldsymbol{r}_Q$, which can be considered as the concentration of the entire primary current in a singular point:

$$\boldsymbol{J}^p(\boldsymbol{r}) = \boldsymbol{Q}\delta(\boldsymbol{r} - \boldsymbol{r}_Q), \tag{2.17}$$

where $\delta(\boldsymbol{r})$ denotes Dirac's Delta function.

2.5.3 Integral formulas for V and B

In order to solve the forward problem, the scalar potential V and the magnetic field $\boldsymbol{B}(\boldsymbol{r})$ resulting from a given primary current distribution $\boldsymbol{J}^p(\boldsymbol{r}')$ have to be computed. Taking the divergence of 2.14 and replacing $\boldsymbol{J}$ by the sum of the primary and the volume current as in equation 2.16, the Poisson equation is found:

$$\begin{aligned} \underbrace{\nabla \cdot \nabla \times \boldsymbol{B}}_{=0} &= \nabla \cdot \Big(\mu_0(\boldsymbol{J}^p - \sigma \nabla V)\Big) \\ \Leftrightarrow \nabla \cdot \boldsymbol{J}^p &= \nabla \cdot (\sigma \nabla V) \end{aligned} \tag{2.18}$$

Once this equation is solved (see section 2.5.4), the Ampère-Laplace law can be used in order to compute the magnetic field at a location $\boldsymbol{r}$, which is caused by a source at $\boldsymbol{r'}$:

$$\boldsymbol{B}(\boldsymbol{r}) = \frac{\mu_0}{4\pi} \int \frac{\boldsymbol{J}(\boldsymbol{r'}) \times \boldsymbol{R}}{R^3} dv' \qquad \text{with } \boldsymbol{R} = \boldsymbol{r} - \boldsymbol{r'} \tag{2.19}$$

With the identities $\frac{\boldsymbol{R}}{R^3} = \nabla' \frac{1}{R}$ and hence $\boldsymbol{J} \times \nabla'(\frac{1}{R}) = \frac{(\nabla' \times \boldsymbol{J})}{R} - \nabla' \times (\frac{\boldsymbol{J}}{R})$, it can be rewritten to

$$\begin{aligned} &= \frac{\mu_0}{4\pi} \int \frac{\nabla' \times \boldsymbol{J}(\boldsymbol{r})}{R} dv' \\ &\overset{2.16}{=} \frac{\mu_0}{4\pi} \Big[\underbrace{\int \frac{\nabla' \times \boldsymbol{J}^p(\boldsymbol{r})}{R} dv'}_{(a)} - \underbrace{\int \frac{\nabla' \sigma \times \nabla' V}{R} dv'}_{(b)} \Big], \end{aligned} \tag{2.20}$$

where term 2.20 (a) and (b) denote the contributions of the primary or volume current respectively. With $\nabla\sigma \times \nabla V = -\nabla \times (V \nabla \sigma)$, it is found that

$$\boldsymbol{B}(\boldsymbol{r}) = \frac{\mu_0}{4\pi} \int (\boldsymbol{J}^p + V \nabla' \sigma) \times \frac{\boldsymbol{R}}{R^3} dv' \tag{2.21}$$

The forward problem hence mainly consists of finding the electric potential V, the computation of the magnetic field is then straight forward. Different methods to solve equation 2.18 exist, such as the Boundary Element Method and the Finite Element Method; for an overview see de Munck, Wolters and Clerc 2012 [12]. The modeling of the head's geometry plays an essential role in these computations. In cases with highly simplified head models (e.g. the spherical model), they can be performed analytically, but for realistically shaped head models numerical methods are needed. Which model is chosen, mainly depends on the question to be answered.

2.5.4 Boundary Element Method

The usage of the BEM requires to model the head's geometry as a piecewise homogeneous conductor. As schematically shown in figure 2.7, different regions G_i $(i = 1...m)$ with conductivites σ_i will be considered. The boundaries between two areas G_i and G_j are denoted as S_{ij} and $\boldsymbol{n}_{ij}(\boldsymbol{r}')$ are the vectors normal to S_{ij} at $\boldsymbol{r}'$. Since the conductivity in G_i is constant, $\nabla \cdot \sigma$ vanishes everywhere except at the boundary surfaces and equation 2.21 can be modified to

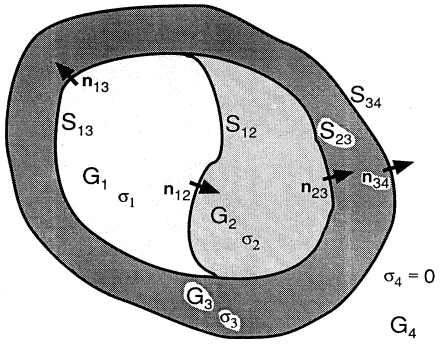

Figure 2.7 Multicompartment conductivity model [20].

$$\boldsymbol{B}(\boldsymbol{r}) = \boldsymbol{B}_0(\boldsymbol{r}) - \frac{\mu_0}{4\pi} \sum_{i=1}^{m} \sigma_i \int\limits_{G_i} \nabla' V \times \frac{\boldsymbol{R}}{R^3} dv', \tag{2.22}$$

where $\boldsymbol{B}_0(\boldsymbol{r})$ is the field produced by the primary current

$$\boldsymbol{B}_0(r) = \frac{\mu_0}{4\pi} \int\limits_{G} \boldsymbol{J}^p(\boldsymbol{r}') \times \frac{\boldsymbol{R}}{R^3} dv'. \tag{2.23}$$

Inserting the identities

$$\nabla \times \left(V \nabla \left(\frac{1}{R} \right) \right) = \nabla V \times \nabla \left(\frac{1}{R} \right) \qquad \text{and}$$
$$\int\limits_{G} \nabla \times \boldsymbol{u} dv = \int\limits_{S} d\boldsymbol{S} \times \boldsymbol{u},$$

with $d\boldsymbol{S}' = \boldsymbol{n}(\boldsymbol{r}')dS'$, the integral in equation 2.22 can be rewritten to

$$\begin{aligned} \int\limits_{G_i} \nabla' V \times \frac{\boldsymbol{R}}{R^3} dv' &= \int\limits_{G_i} \nabla' V \times \nabla' \frac{1}{R} dv' \\ &= - \int\limits_{\partial G_i} V \nabla' \frac{1}{R} \times d\boldsymbol{S}' \end{aligned} \tag{2.24}$$

and results in

$$\boldsymbol{B}(\boldsymbol{r}) = \boldsymbol{B}_0(\boldsymbol{r}) + \frac{\mu_0}{4\pi} \Sigma'_{ij} (\sigma_i - \sigma_j) \int\limits_{S_{ij}} V(\boldsymbol{r}') \frac{\boldsymbol{R}}{R^3} \times d\boldsymbol{S}'_{ij}. \tag{2.25}$$

The prime signifies summation over all boundaries. To solve the simplified equation for the magnetic field, the electric potential on the boundary surfaces is needed. An integral equation

for V can be obtained by using Green's second identity (see [20] for details):

$$(\sigma_i + \sigma_j)V(\boldsymbol{r}) = 2\sigma_0 V_0(\boldsymbol{r}) + \frac{1}{2\pi}\Sigma'_{ij}(\sigma_i - \sigma_j)\int\limits_{S_{ij}} V(\boldsymbol{r}')d\Omega_r(\boldsymbol{r}') \qquad \text{with} \tag{2.26}$$

$$d\Omega_r(\boldsymbol{r}') = -|\boldsymbol{r} - \boldsymbol{r}'|^{-3}(\boldsymbol{r} - \boldsymbol{r}') \cdot d\boldsymbol{S}'_{ij}.$$

In order to solve for the potential, the considered surfaces S_i are tesselated into suitable triangles, which are assumed to have a constant potential. This original formulation of the BEM has been further developed and numerically implemented. The most common methods to solve the problem are the double-layer approach and the symmetric approach, which was developed by Kybic et al. in 2005 [25] and implemented in OpenMEEG by Gramfort et al. in 2010 [18]. Since the symmetric approach has been shown to have the highest accuracy, it is chosen for this thesis. For further details of this method it is referred to the mentioned publications [18, 25].
Once the potential V and the corresponding magnetic field B for any possible dipole location $\boldsymbol{r}_Q$ are computed, vector fields $\boldsymbol{L}_V$ and $\boldsymbol{L}_B$ can be found fulfilling

$$B_i = \int \boldsymbol{L}_i^B(\boldsymbol{r}) \cdot \boldsymbol{J}^p(\boldsymbol{r})dv \tag{2.27}$$

$$V_i = \int \boldsymbol{L}_i^V(\boldsymbol{r}) \cdot \boldsymbol{J}^p(\boldsymbol{r})dv, \tag{2.28}$$

which are called lead fields and define the starting point for solving the inverse problem [20].

2.6 The Inverse Problem: Dynamic Statistical Parametric Mapping (dSPM)

The inverse method called dynamic Statistical Parametric Mapping (dSPM) was developed in 2000 by Dale et al. [10] as an improvement to the linear source estimation approach suggested in [11]. Let

$$\boldsymbol{x} = \begin{bmatrix} \boldsymbol{V} \\ \boldsymbol{B} \end{bmatrix} \qquad \boldsymbol{A} = \begin{bmatrix} \boldsymbol{L}^V \\ \boldsymbol{L}^B \end{bmatrix}$$

be the combined measured electric potential $\boldsymbol{V}$ and magnetic field $\boldsymbol{B}$ and the corresponding combined lead field respectively. After solving the forward problem, some additive noise can be assumed in the actual recordings. The recorded data can therefore be expressed as

$$\boldsymbol{x} = \boldsymbol{A}\boldsymbol{s} + \boldsymbol{n} \tag{2.29}$$

where $\boldsymbol{s}$ denotes the dipole strength and $\boldsymbol{n}$ the noise. The next step is to solve the inverse problem, meaning to deduce the strength of the dipoles $\boldsymbol{s}$ from the recorded sensor data $\boldsymbol{x}$. Since the solution to this problem is not well-defined, a priori information about the statistical

distribution of dipole moment and sensor noise are needed to express the problem in terms of statistical estimation theory. For a linear case, this means minimizing the expected difference between the estimated solution $\hat{\boldsymbol{s}}$ and the correct solution $\boldsymbol{s}$, which can be expressed as

$$Err_{\boldsymbol{W}} = \langle \|\hat{\boldsymbol{s}} - \boldsymbol{s}\|^2 \rangle = \langle \|\boldsymbol{W}\boldsymbol{x} - \boldsymbol{s}\|^2 \rangle, \tag{2.30}$$

with $\boldsymbol{W}$ being the linear operator, mapping a vector $\boldsymbol{x}$ into $\hat{\boldsymbol{s}}$, and $\langle ... \rangle$ denoting the expectation value. Assuming normal distributions with zero mean for $\boldsymbol{n}$ and $\boldsymbol{s}$, equation 2.30 can be rewritten to

$$\begin{aligned} Err_{\boldsymbol{W}} &= \langle \|\boldsymbol{W}(\boldsymbol{A}\boldsymbol{s} + \boldsymbol{n}) - \boldsymbol{s}\|^2 \rangle \\ &= \langle \|(\boldsymbol{W}\boldsymbol{A} - \boldsymbol{I})\boldsymbol{s} + \boldsymbol{W}\boldsymbol{n}\|^2 \rangle \\ &= \langle \|\boldsymbol{M}\boldsymbol{s} + \boldsymbol{W}\boldsymbol{n}\|^2 \rangle, \qquad \text{where } \boldsymbol{M} = \boldsymbol{W}\boldsymbol{A} - \boldsymbol{I} \\ &= \langle \|\boldsymbol{M}\boldsymbol{s}\|^2 \rangle + \langle \|\boldsymbol{W}\boldsymbol{n}\|^2 \rangle \\ &= Tr(\boldsymbol{M}\boldsymbol{R}\boldsymbol{M}^T) + Tr(\boldsymbol{W}\boldsymbol{C}\boldsymbol{W}^{\boldsymbol{T}}), \end{aligned} \tag{2.31}$$

where $\boldsymbol{C} = \langle \boldsymbol{n}(t)\boldsymbol{n}(t)^T \rangle$ and $\boldsymbol{R} = \langle \boldsymbol{s}(t)\boldsymbol{s}(t)^T \rangle$ are the covariance matrices of the noise and the dipole strength respectively. Minimizing the error with respect to $\boldsymbol{W}$, the optimal estimate is given by

$$\begin{aligned} \hat{\boldsymbol{s}} &= \boldsymbol{W}\boldsymbol{x}(t) \qquad \text{with} \\ \boldsymbol{W} &= \boldsymbol{R}\boldsymbol{A}^T(\boldsymbol{A}\boldsymbol{R}\boldsymbol{A}^{\boldsymbol{T}} + \boldsymbol{C})^{-1}, \end{aligned} \tag{2.32}$$

which is equivalent to the Minimum Norm Estimate (MNE) [21] in the case of $\boldsymbol{C}$ and $\boldsymbol{R}$ being proportional to the identity. However, this formulation permits to include empirical observations or assumptions about the second order statistics of the sensor noise and the dipole strengths in order to constrain the solution.

One approach to include such a constraint and remove the bias for superficial sources resulting from the MNE approach was suggested by Dale et al. [10], who included fMRI data as additional prior information with the goal to determine the pattern of electrical activity that is most consistent with all recorded data (EEG, MEG and fMRI). With the Bayesian theorem, this goal can be expressed as the maximum of the posterior distribution

$$P\Big(\boldsymbol{j}(\boldsymbol{r},t)|\boldsymbol{x}(t), f(\boldsymbol{r},t)\Big) = \frac{P\Big(\boldsymbol{x}(t)|\boldsymbol{j}(\boldsymbol{r},t)\Big)P\Big(f(\boldsymbol{r},t)|\boldsymbol{j}(\boldsymbol{r},t)\Big)P\Big(\boldsymbol{j}(\boldsymbol{r},t)\Big)}{P\Big(\boldsymbol{x}(t), f(\boldsymbol{r},t)\Big)}, \tag{2.33}$$

where as before, $\boldsymbol{x}(t)$ denotes the EEG-MEG recordings, $\boldsymbol{j}(\boldsymbol{r},t)$ the current dipole vector and $f(\boldsymbol{r},t)$ describes the fMRI signal strength at certain location and time point. The term $P\Big(\boldsymbol{x}(t)|\boldsymbol{j}(\boldsymbol{r},t)\Big)$ corresponds to the forward solution of EEG and MEG $\boldsymbol{x} = \boldsymbol{A}\boldsymbol{s} + \boldsymbol{n}$, as dis-

cussed above. The term $P\Big(f(\boldsymbol{r},t)|\boldsymbol{j}(\boldsymbol{r},t)\Big)$ analogously describes the coupling between the spatiotemporal pattern of electrical activity and the fMRI signal. The prior $P\Big(\boldsymbol{j}(\boldsymbol{r},t)\Big)$ describes the a priori likelihood for different spatiotemporal patterns of dipole strenghts and therefore offers the possibility to include knowledge about the distribution of the electric activity within the brain. Their foundational assumption in order to spatially bias the resulting estimate is a strong correlation between the spatial pattern of the electromagnetic response and the hemodynamic measures conducted by fMRI.
It can be shown that the maximum of the posterior distribution in equation 2.33 is equivalent to the minimum of the error discussed above (equation 2.32). Further information about the dipole strength variance and covariance as a function of the local fMRI response can be encoded in $\boldsymbol{R}$. It is a common method to present fMRI activation as a noise-normalized statistical parametric map. A similar map can be obtained by normalizing the estimates by predicted estimator noise. The variance of each dipole strength estimate is given by

$$Var(\hat{\boldsymbol{s}}_i) = \langle(\boldsymbol{w}_i\boldsymbol{n}(t))^2\rangle = \boldsymbol{w}_i\boldsymbol{C}\boldsymbol{w}_i^T. \tag{2.34}$$

The noise normalization then leads to

$$z_i(t) = \frac{\boldsymbol{w}_i \cdot \boldsymbol{x}(t)}{\sqrt{\boldsymbol{w}_i\boldsymbol{C}\boldsymbol{w}_i^T}}, \tag{2.35}$$

which is a unitless measure of the source activity, assuming that the source orientation is fixed as normal to the cortex.

3 Materials and Methods

Several sets of data were recorded in order to answer the fundamental question of this thesis. All data was collected between June and October 2020. Due to the ongoing Covid-19 pandemic, a hygienic protocol[6] was followed strictly, to endanger neither the subjects nor the staff.

3.1 Participants

The final sample consists of 4 men and 4 women with a mean age of 25.5 years (SD: 2.7 years), ranging from 21 to 29. All of them were normal-hearing, all but one (subject 7) were right-handed. The participation in the study was voluntary and ethical clearance was obtained by the ethics committee of the Friedrich-Alexander Universität Erlangen-Nürnberg (Ref No 4453 B). Participants were informed about the experimental procedure before the measurement, however the goal of the study was only revealed after.

3.2 Stimulus

There are different possibilities to stimulate subjects in order to observe the ASSR. For this study, the stimulus consists of sinusoidal amplitude modulated tones, since they evoke the most frequency specific response [24]. They are described by the function

$$y(t) = a \cdot \sin\Big(2\pi f_c t\Big) \cdot \Big(1 - m\cos(2\pi f_m t)\Big) \tag{3.1}$$

with a being the amplitude, m the modulation depth, f_c and f_m the carrier or the modulation frequency respectively. Setting $a = 1$ and $m = 1$ and using the basic trigonometric identity

$$\sin(a)\cos(b) = \frac{\sin(a+b) + \sin(a-b)}{2},$$

equation 3.1 can be rewritten to

$$y(t) = \sin(2\pi f_c t) - \frac{1}{2}\Big[\sin\Big(2\pi(f_c + f_m)t\Big) + \sin\Big(2\pi(f_c - f_m)t\Big)\Big]. \tag{3.2}$$

It shows, that the sound consists of one main oscillation at the carrier frequency f_c and two side bands at the frequencies $f_c + f_m$ and $f_c - f_m$. A simulation of the stimulus in time and frequency domain is visualized in figure 3.1a. Based on Ross et al. [33], low carrier frequencies elicit higher signals. Hence 500 Hz was chosen as a compromise to utilize a relatively low carrier frequency and still being able to avoid noise when transferring the sound to the subject's ears.

[6] The protocol fulfilled all requirements that were imposed by the German Government and the director of the University of Münster by the time.

17 modulation frequencies were measured in 4 runs, ranging from 16 Hz to 61 Hz (see table 1)[7]. The MFs were chosen based on different criteria: ranges, which based on literature promised to be of high interest, were scanned with a higher density than others. Furthermore, frequencies with an inherent technical noise, namely 50 Hz (line noise) and 37.5 Hz (for details see chapter 3.4.3) were avoided in a sufficiently large range. Each MF appeared 3 times in the corresponding run in a pseudo-randomized order. The sounds lasted 25s with a subsequent pause of 8 seconds and were generated with Psychtoolbox 3 [7].

Table 1 Utilized MFs in Hertz in 4 runs. The blue values show the MFs for subject 4, the black values correspond to all other subjects. The rows indicate the runs, in which they were measured.

	MF1	MF2	MF3	MF4	MF5	MF6
1	16 21	24 25	39 36	40 40	47 44	48
2	18 22	28 28	40 37	41 41	53 45	52
3	20 23	32 31	40 38	43 42	57 46	55
4	22 24	36 33	40 39	45 43	61 47	58

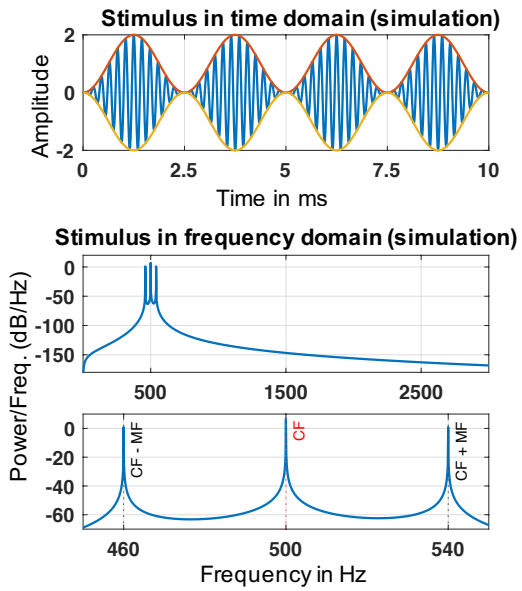

(a) Simulation of a 40 Hz amplitude modulated sinusoidal tone
upper: in the time domain.
middle: in the frequency domain: exactly three peaks are visible.
lower: in the frequency domain (enlarged presentation): as expected, the main peak occurs at the carrier frequency of 500 Hz and the side bands 40 Hz higher or lower respectively.

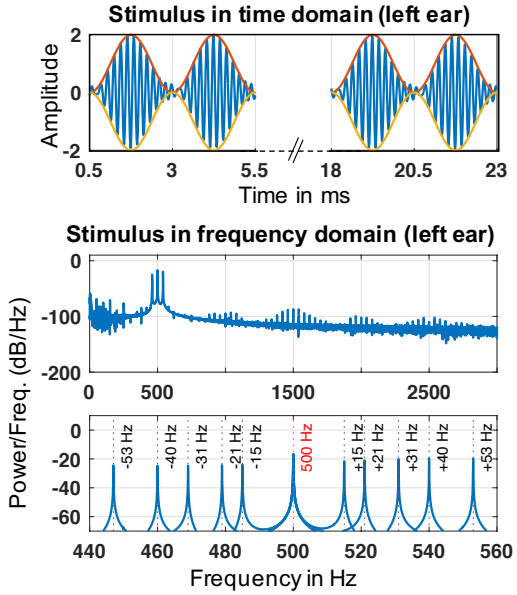

(b) Recordings of a 40 Hz amplitude modulated sinusoidal tone
upper: in the time domain.
middle: in the frequency domain: three peaks are visible and some negligible noise.
lower: in the frequency domain (enlarged presentation, several MFs plotted): as expected, the main peak occurs at the carrier frequency of 500 Hz and the side bands higher or lower respectively, the difference corresponding exactly to the MF.

Figure 3.1 Presentation of **(a)** the simulated and **(b)** the recorded stimulus in time and frequency domain.

No electric devices can be inside the magnetically shielded room, because it would lead

[7]For subject 4, a different set of MFs was used, ranging from 21 Hz to 58 Hz (see blue values in table 1). The results found in this first measurement indicated, that the frequency range should be extended. Nevertheless, the data were included in the analysis.

to noise in the MEG recordings. Therefore, the sound was generated outside of the room and transported via airtubes to the subject's ears. To ensure that the sound was transferred correctly, a test recording of the sound has been conducted. An artifical ear was connected to the airtube with an integrated microphone in order to record the sound, that the participants will hear. A brief analysis of the recorded sound is presented in figure 3.1b. It shows the recorded sound (blue), and the enveloping oscillation (orange and yellow), which is stable over time. Small deviations compared to the simulation can be seen in the areas, where the amplitude of the envelope approaches zero, but they can be neglected, since they are comparatively small and furthermore it is not required to have a modulation depth of 100% in order to elicit the ASSR. In the frequency domain, some small peaks can be seen, but they can all be considered negligible noise, since they are a lot smaller than the peaks of interest (note that the y-axis is scaled in decibel).
While some studies claim, that the level of attention in a wake state does not influence the result of the ASSR (e.g. [13, 29]), other studies have shown a difference in the ASSR between attentive and non-attentive states (e.g. [35]). In order to avoid a potential influence of the subject's attention, a constant level of wakefulness and attention has been ensured by the inclusion of a vigilance task: different endings of the sound, either abrupt or fading, had to be identified. In the case of a fade-out (33% of all cases), a button had to be pressed with the right index finger, while no action was required in the case of an abrupt ending.

3.3 Measures and Procedure

EEG, MEG, MRI[8] and ECG data were required for this study. 56 AgCl sintered EEG ring electrodes (EASYCAP GmbH, Germany) were distributed on the subject's head. The arrangement corresponds to a 10-20-system and the electrode FCz served as the reference. In order to improve the conductivity, a gel was applied. The exact positions of the electrodes and the head shape were digitized with a Polhemus device (FASTRAK, Polhemus Incorporated, USA), enabling a registration between the different modalities. MEG data was recorded with 275 axial gradiometers (OMEGA2005, VSM MedTech Ltd., Canada). The subject's head movement during the measurement was measured with three head localization coils on nasion and the left/right preauricular points and kept below 5mm. In addition, the Electrocardiogram was measured in order to clean the data from the heartbeat induced noise. Before the measurement started, the subject's hearing threshold for amplitude modulated sound of 500 Hz carrier frequency and 40 Hz modulation frequency was determined for both ears individually. The sound was then presented 55 dB above this threshold and it was ensured, that the subject indeed perceives the sound at the same volume in both ears. The 4 runs (cf. table 1) were recorded in one session, between each two runs, the subjects were asked to take a short break and it was ensured that the subject still sits properly in the MEG.

[8]This measurement was not conducted by the author.

3.4 Data Analysis

The data analysis was performed in Brainstorm and Matlab. Conducted steps were based on the Brainstorm tutorial and previous studies about the ASSR. The goal of the analysis is to obtain graphs, which show the strength of the ASSR depending on the modulation frequency, the so-called ASSR profiles. The maximum of the diagonal ASSR profile is referred to as the *resonance frequency*.

3.4.1 Brainstorm

Brainstorm [39] is an open-source tool specialized on the analysis of different kinds of brain data. It is a Matlab toolbox, combining many different neuroscientific toolboxes in one environment, allowing scripting while also having a graphic user interface. One goal of this study is to explore the options, that Brainstorm offers in data analysis. The entire pipeline, starting from raw data analysis, preprocessing and MRI segmentation, leading to source analysis was built in the Matlab-Brainstorm environment.

3.4.2 MRI Segmentation and Head Model

T1-weighted MRI data was available for all subjects from previous studies and therefore did not have to be recorded. The T1-MRIs were segmented by the CAT12 algorithm [17], which is also accessible via Brainstorm. The cortex was modeled by 15000 vertices, which will later be the possible locations of sources. From the computed segmentation, the three BEM surfaces, namely head, outer and inner skull were created, with Brainstorm's default option of 1922 vertices per layer.

3.4.3 Data-Preprocessing of Functional Data

Raw EEG and MEG data does not only contain the signal, but also noise from different sources. Before starting the analysis, it is important to minimize the noise, while keeping the signal. Hence, only noise, that could be identified from a non-cerebral source, was removed and includes eye-blinks, heartbeat, electric current noise and SQUID jumps.

Data filtering

First, Welch's Power Spectrum [47] of the raw data was computed for each run. By manually inspecting the data in the time and the frequency domain, bad channels and bad time segments were identified and rejected. Subsequently, a bandpass filter (1 Hz to 120 Hz) and a notch filter (50Hz, 100Hz) were applied in order to correct for linear trends and the line noise from the European Voltage system respectively (see figures 3.2a, 3.2b). Resulting transients in the beginning and the end of continuous data file were excluded from further analysis.

Independent Component Analysis

In addition, an Independent Component Analysis (ICA) was performed in order to remove eye-

blink and heartbeat artifacts. The ICA-components were sorted by strength of the correlation to EEG-sensors close to the eyes (Fp1, Fp2) and to the ECG signal, in order to identify components containing artifacts resulting from eye-blinks and the heartbeat, which were then deleted. Components were only deleted under the condition that they do not contain too much other signal. To ensure this, both the signal in time and the topography of the components were inspected manually. By default, 20 components were computed and in most cases found sufficient in order to identify clear eye- and ECG-components. If this was not the case, another ICA was run with 40 components. Eventually, eye-blink components were deleted for in each modality, EEG and MEG, while the heartbeat component was only deleted for MEG (since it was a lot weaker in the EEG) for all subjects.

Remove SQUID Jumps

Some of the data showed SQUID jumps, which show as steps with a large amplitude (comparable to the Heaviside function) that results in a change of baseline in one or more channels (see figure 3.2g). Although the baseline of MEG data is arbitrary, SQUID jumps cause problems in further processing the continuous data. Due to the sharp nature of the jump, the artifact, that originally has a size of few milliseconds is growing to an extent of several seconds when filtering is applied. The data of this long section would then have to be excluded from the analysis. In order to minimize the rejected data, the following procedure was applied: If the jump only showed in one or two magnetometers, the corresponding channels were marked as bad. If this wasn't reasonable, because several sensors contained the SQUID jump, in a first step, the start (t_1) and the end (t_2) of the jump were defined manually. The median value of the 10 seconds before t_1 (or after t_2 respectively) were subtracted from each time point for each channel in the corresponding section in order to bring the baselines to a similar level. The data of the jump ± 50 sample points were omitted and replaced by data generated by an interpolation algorithm. This interpolated time segment does not contain the real brain activity and will therefore be excluded from the data analysis, but it is not longer than $\approx 300\,\text{ms}$ and will not spread when applying filters. Hence, several seconds of data can be saved by this procedure. The results of this procedure are presented in figure 3.2h. Before the data was finally segmented into epochs, the cleaned continuous data files and their power spectra were inspected once more to ensure all artifacts were either filtered out or marked as bad. After this process, epochs were imported from a time window from -8s to 25s, where time point 0 is the onset of the corresponding sound with a corrected baseline.

Even though many sources of noise have already been eliminated, some still remain which cannot be removed. One large artifact in the MEG data results from the EEG-cap and elicits non-cerebral activity close to the right temporal lobe. This noise is difficult to remove since it concerns many sensors in the same area, that cannot all be rejected. Since this artifact is frequency specific at 37.5 Hz (and harmonics), the analysis is conducted in a way that it

doesn't influence the results[9].

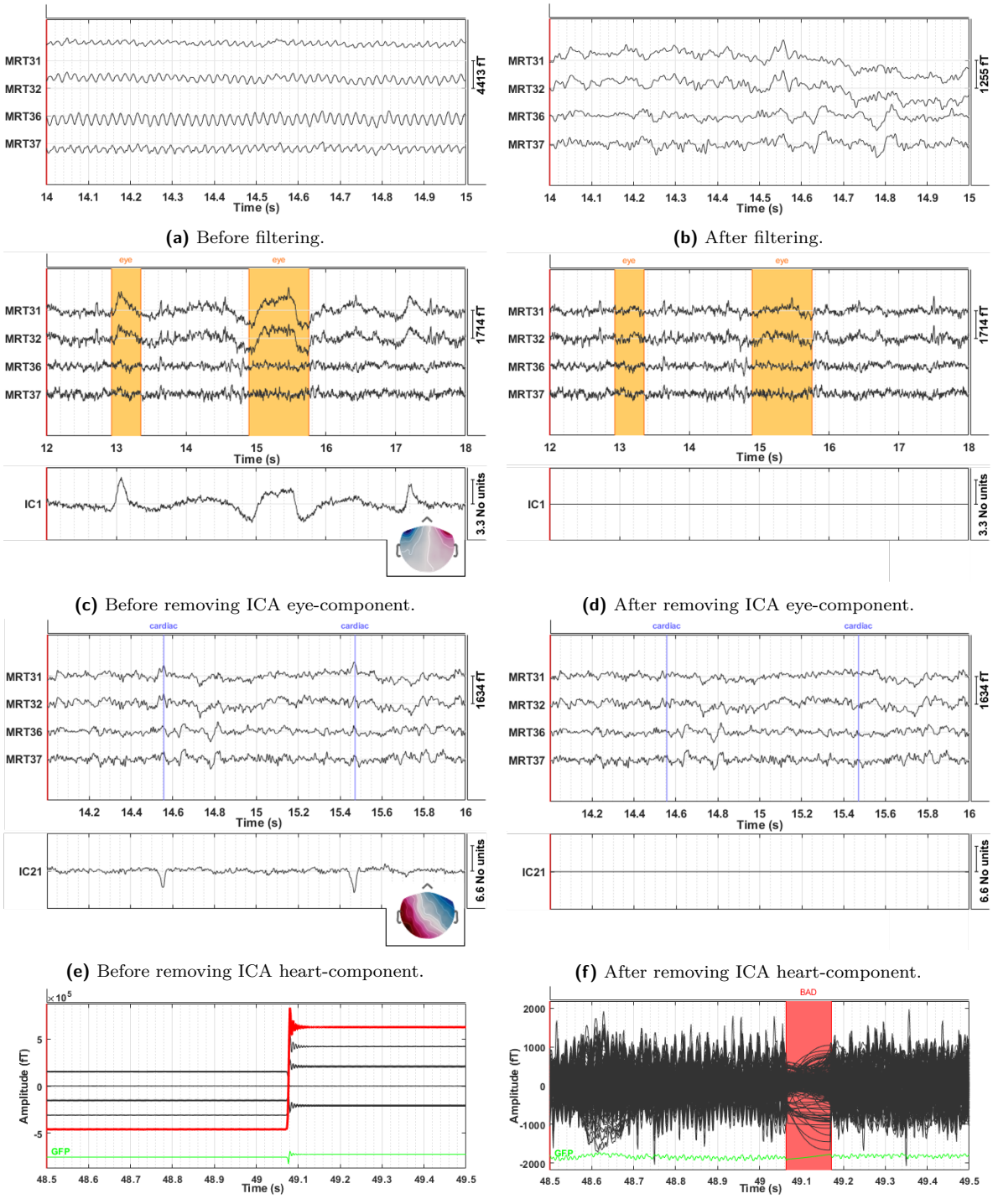

(a) Before filtering.

(b) After filtering.

(c) Before removing ICA eye-component.

(d) After removing ICA eye-component.

(e) Before removing ICA heart-component.

(f) After removing ICA heart-component.

(g) Before correcting squid jump

(h) After correcting squid jump

Figure 3.2 Four steps of data preprocessing. Steps in rows 1-3 were applied for every subject, while the step in row 4 was only applied where necessary.

[9]A similar procedure could have been used for the line noise, but since it is very strong, the cleansing process would have been difficult to perform.

3.4.4 EEG-Analysis on Sensor Level

The analysis of the EEG data was conducted on the sensor level, meaning that all steps described in this section were performed on each channel individually. Further, the analysis in the time domain was avoided, due to possible phase imperfections, leading to undesired signal cancelling.

The final EEG-data consists of 33s epochs, containing 8s recordings before and 25s after stimulus onset, as presented in figure 3.3. Two different kinds of Power Spectra were computed: The first one is a baseline spectrum, S_{baseline}(one per run) computed from all baseline data segments [-6s, 0s] in the corresponding run. The second kind is the signal spectrum S_{signal} (one per MF), computed from all signal data segments [0.5s, 24.5s] of the corresponding modulation frequency. Since the ASSR only evolves around 240 ms after the stimulus onset and some aftereffects at the stimulus offset might occur, the rest of the data in each epoch was discarded. Both spectrum types were computed from 2s data windows with an overlap of 50%, resulting in up to 75 averaged spectra in the baseline spectrum and up to 69 in the signal spectrum (given that no epochs were excluded due to artifacts) with a resolution of 0.5 Hz. As explained in section 2.2, the frequency spectra EEG and MEG data have an aperiodic background. In order to compare the spectra of the different MFs, a correction of this background has to take place. What is of interest, is the change of the power between the baseline and the signal. Two different methods of baseline correction are compared: The absolute difference spectrum (ADS) obtained by

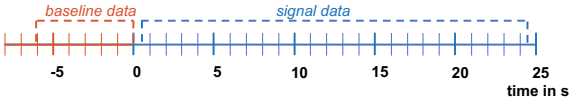

Figure 3.3 Time course of a single epoch with the sound onset at 0s.

$$ADS = S_{\text{signal}} - S_{\text{baseline}}$$

and a relative difference spectrum (RDS) obtained by

$$RDS = \frac{S_{\text{signal}} - S_{\text{baseline}}}{S_{\text{baseline}}} \cdot 100.$$

From the resulting difference spectra (one per MF), five EEG electrodes (AFz, Fz, FCz, Cz, CPz) were compared and the one eliciting the highest signal at 40 Hz was chosen to be analyzed. The power values at the MF were extracted from the ADS and RDS respectively and plotted against the corresponding MF, resulting in the ASSR profiles. Since the condition 40 Hz was measured in every run, the average value of all runs was considered for this case. The frequency bins in the vicinity of the MF serve as an estimate for the noise background: The absolute amplitudes of the ADS/RDS at MF $\pm$ 1 Hz, MF $\pm$ 1.5 Hz and MF $\pm$ 2 Hz were extracted and averaged. In order to deduct the resonance frequency from the ASSR profile, the extracted values were low pass filtered with a bidirectional moving average filter. The maximum of the filtered profile was considered the resonance frequency.

3.4.5 MEG-Analysis on Source Level

As a second approach to identify the resonance frequency, the MEG data were analyzed on a source level, similar to the analysis conducted by Ross et al. [33]. Since in contrast to Ross' study, MEG data were available for the entire head, a separate analysis for both hemispheres was performed.

Source localization

Before the source strength can be analyzed in the frequency domain, the location of the source has to be defined. Therefore, based on the three compartment head model, the forward problem was solved, using Brainstorm's recommended conductivity parameters 0.0125 for the skull and 1 for the scalp and brain [10]. The adaptive integration method was chosen. Subsequently, the source analysis was conducted with dSPM. Since the computation of the sources was based on non-averaged data, the SNR was estimated to be 1. A noise covariance matrix was computed from the baseline segments of the data. The orientation of the sources was fixed to be normal to the cortex; recommended parameters for noise covariance regularization (0.1) and depth weighting (0.5)[11] were kept. An inverse kernel was computed, which, multiplied with a data segment, shows the strength of the sources in all vertices of the cortex over time. Analogously to the sensor data, the source data can be transferred from the time domain into the frequency domain. Again, no averaging in the time domain was performed in order to avoid signal cancelling.
Since the stimulation frequencies only differ in a range of 439 Hz to 561 Hz (see section 3.2), no detectable tonotopic organization is expected [27], hence the localization of the source was limited to one modulation frequency. Based on literature, a strong signal of the ASSR is expected around 40 Hz, hence the localization will be performed on this modulation frequency. To do so, 2s segments of the 40-Hz signal and all baselines in all runs were extracted from the long epochs with an overlap of 50%. The fourier transforms of the source waveforms were computed for the entire cortex. A non-parametric permutation Student's t-test for unequal variances (5000 randomizations) was performed on the two sets of data for each subject, since on a source level, it is legitimate to do inter-run-computations. The result is a cortical map, that shows all vertices with a statistically significant ($p<0.01$) difference between the signal and the baseline at 40 Hz. The maximum of the source amplitude was evaluated for both hemispheres individually and all vertices with at least 65% of this maximum amplitude were defined as the region of interest, resulting in two scouts, one for each hemisphere. It might be a matter of discussion whether it is legitimate to exclude vertices that have shown a significant difference between signal and baseline. However, in the case of this analysis, the source's absolute strength is not of interest, but the qualitative change of the source amplitude for

[10] The parameters are implemented unitless and in a way that only their ratio matters.
[11] Since dSPM is inherently considering depth weighting, it is not expected to influence the results much.

different modulation frequencies. Therefore, limiting the analysis to vertices with a high amplitude leads to a clearer signal with less noise and the qualitative behaviour is not expected to be affected by this.

Power Spectrum Analysis

Once the source was localized, the difference spectra of the scout were calculated for each modulation frequency and hemisphere. Strictly spoken, one spectrum per vertex was computed, which were then averaged in order to obtain a spectrum of the scout. Analogously to the EEG-sensors analysis, time windows were chosen as 2s width with an overlap of 50%, resulting in a Power Spectrum with 0.5 Hz resolution. Further processing to obtain the ASSR profile was equivalent to the procedure in the EEG Sensor Analysis.

4 Results

All results are presented in the following sections. Since the analysis is conducted on an individual level, results are always presented per subject, not in a grand averages. Depending on the relevance of the specific result, it might only be illustrated by the results of one subject or all subjects are presented. Further results can be obtained by the author, if needed. First, the results of the EEG sensor analysis are presented in section 4.1. A brief MEG sensor analysis follows in section 4.2 for a more holistic understanding and some further insights on the data, before finally conducting the source analysis in section 4.3. The resonance frequencies determined in those chapters will be compared in section 4.4.

4.1 EEG-Analysis on Sensor Level

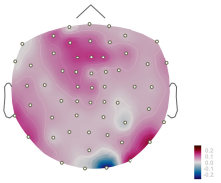

(a) Topography of the absolute difference spectrum at 40 Hz.

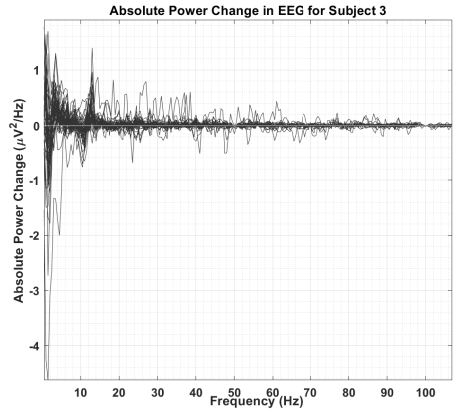

(b) Absolute difference spectrum for all electrodes.

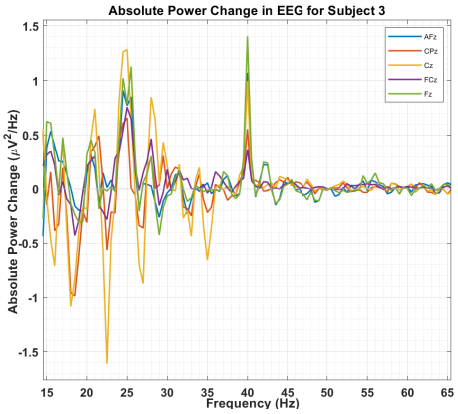

(c) Absolute difference spectrum for relevant electrodes.

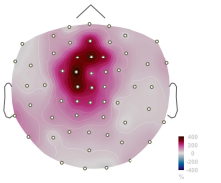

(d) Topography of the relative difference spectrum at 40 Hz.

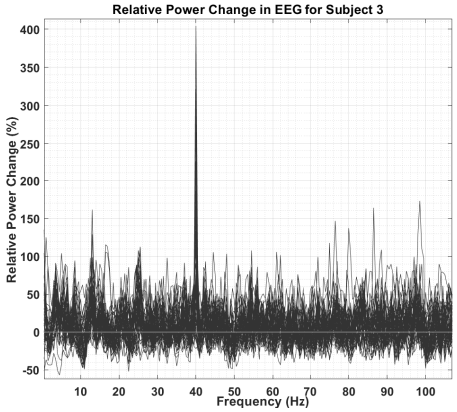

(e) Relative difference spectrum for all electrodes.

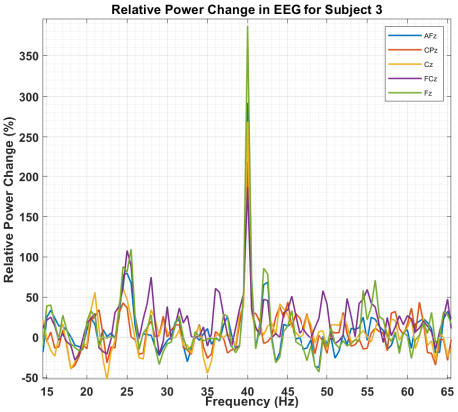

(f) Relative difference spectrum for relevant electrodes.

Figure 4.1 Absolute (a-c) and relative (d-f) change in EEG sensor power for subject 3 at a MF of 40 Hz. The topographies in (a) and (d) show the increased activity at 40 Hz during the stimulation, which is much clearer in the case of relative baseline correction. The ADS for all electrodes in (b) is too noisy to see the 40 Hz-peak, the RDS in (e) shows a clear peak at the MF. If only the relevant electrodes are plotted, as in (c) and (f), a peak at the modulation frequency is visible for both modalities.

Typical results of an absolute and a relative difference spectrum of a specific modulation frequency (here 40 Hz) for EEG sensors are presented in figure 4.1. The topographies in 4.1a and 4.1d show an expected enhanced activity in the frontal lobe, which is much clearer in the relative than the absolute case. The activity of the two hemispheres can not be distinguished by the EEG-topography, since they fuse in the central area. Furthermore, the counterparts of the expected dipoles are not visible, since they are located in the neck area, where no electrodes were placed. The difference spectra for all electrodes in 4.1b and 4.1e confirm the behaviour observed in the topographies: a clear peak is visible in the relative spectrum, but none can be detected in the absolute spectrum. Therefore, the difference spectra of the relevant electrodes are presented in figures 4.1c and 4.1f, which both show a peak at the modulation frequency.

The electrode with the highest value is determined as described in section 4.1 and the ASSR values are extracted at each modulation frequency to create the ASSR profiles in figures 4.2 and 4.3.
For the absolute ASSR profiles, all subjects showed the highest amplitude in the electrode Fz. The qualitative behaviour of the profiles can be classified into 3 categories: Subjects 1, 3 and 6 show a peak in the vicinity of 40 Hz, as is expected from the literature. Amplitudes increase for modulation frequencies below 20 Hz, but are not or only barely distinguishable from the noise background. Subjects 5 and 7 show the maximum at a lower modulation frequency and decay slowly for higher frequencies. Again, the ASSR for low frequencies cannot be distinguished from the background. For subject 2, no ASSR profile can be distinguished from the estimated noise background and also subjects 4 and 8 show a very bad signal to noise ratio. The overall impression of the obtained ASSR profiles is very noisy.
Slightly cleaner results are found in the relative ASSR profiles. Here, the electrode with the highest amplitude varies between subjects and is indicated in the title of the plot. The dominant noise in the low frequencies of the absolute ASSR profiles disappears and subjects 1, 3, 5, 6 and 7 show a maximum close to 40 Hz with a high SNR. Subject 8 also shows a larger SNR and an increasing tendency of the amplitude for higher modulation frequencies is visible. Subjects 2 and 4 still show a very low SNR and the values of the relative change in power is below 100%.

For the analysis of the resonance frequencies, which are indicated by the green bars in each ASSR profile, see section 4.4.

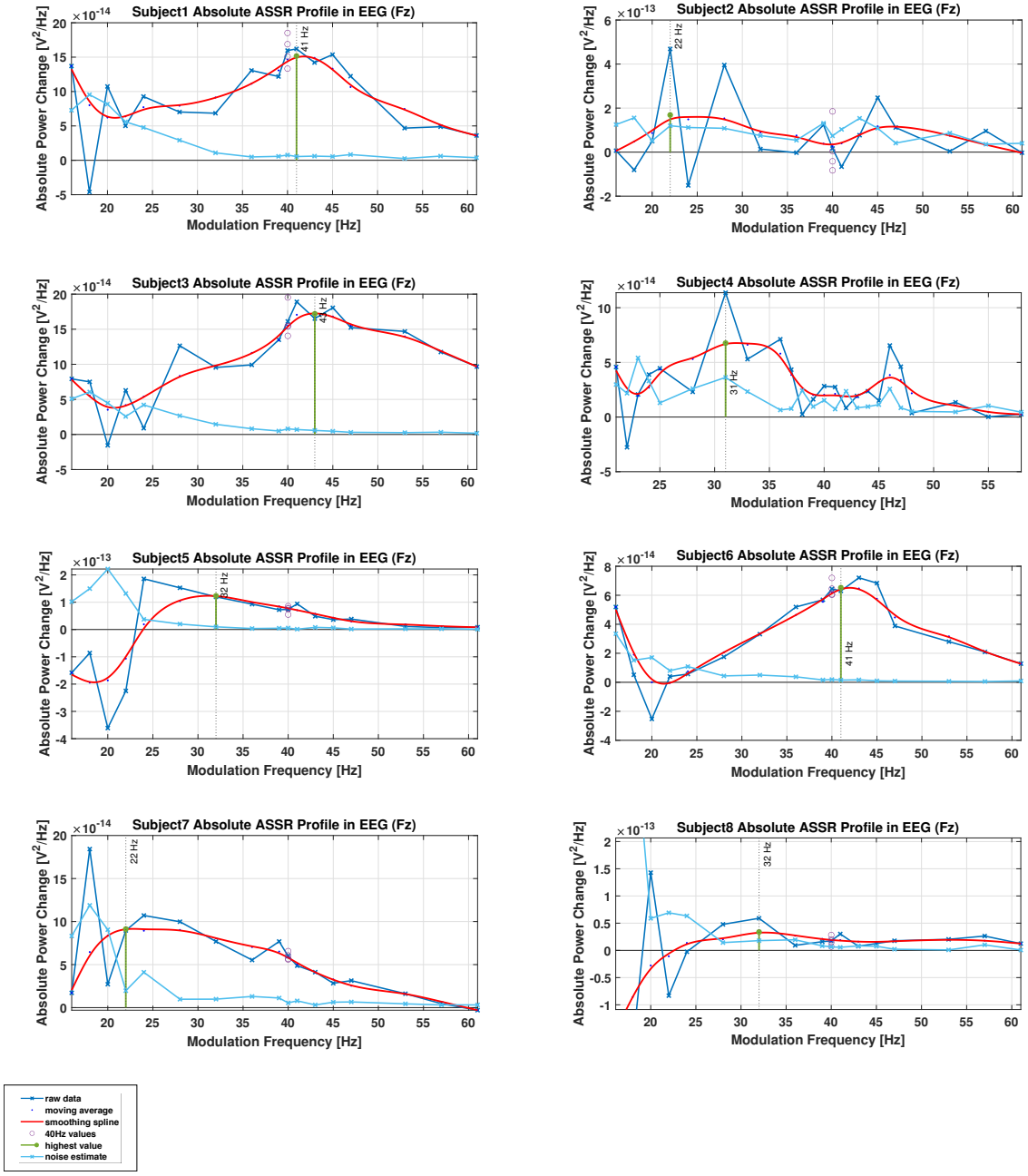

Figure 4.2 Absolute ASSR profiles in EEG sensors. The maximal value was obtained at electrode Fz for all subjects. The raw data is marked in blue, the smoothed data is presented in red. An estimate of the noise is given in light blue, the maximum of the smoothed data is indicated by a green bar. Single values for 40 Hz are indicated in purple (despite subject 4). Subjects 1, 3 and 6 show a peak of the profile amplitude at around 40 Hz. For frequencies below 20 Hz, the values increase, but the amplitudes get almost indistinguishable from the noise background. Subjects 5 and 7 show the maximum of the profile for lower frequencies (22 Hz and 32 Hz) and decay slowly for increasing modulation frequencies. The profiles of Subjects 2, 4 and 8 can not or barely be distinguished from the noise background.

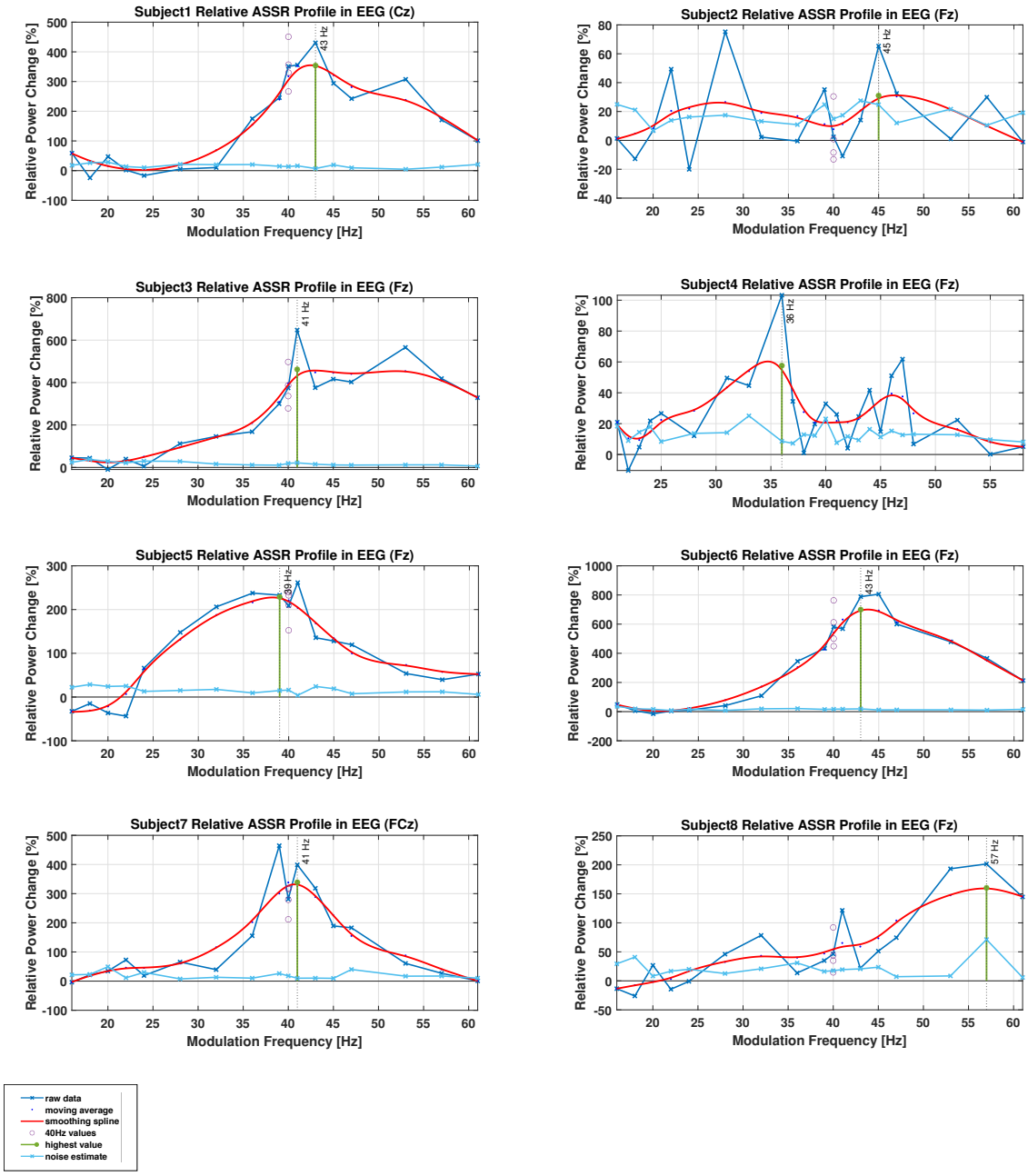

Figure 4.3 Relative ASSR profile in EEG sensors. The electrodes with the highest amplitude varies between subjects. The raw data is marked in blue, the smoothed data is presented in red. An estimate of the noise is given in light blue, the maximum of the smoothed data is indicated by a green bar. Single values for 40 Hz are indicated in purple (despite subject 4). Subjects 1, 3, 5, 6 and 7 show a peak of the profile amplitude at around 40 Hz. Subject 8 shows the maximum of the profile for a higher frequency (57 Hz). The profiles of Subjects 2 and 4 can not or barely be distinguished from the noise background and show amplitudes of less than 100%.

4.2 (Brief) MEG-Analysis on Sensor Level

Although the analysis of the MEG data will mainly be performed on the source level, some findings on the sensor level will be presented, which contribute to a more holistic impression of the data, link to other studies performed on the sensor level and improve the general understanding. It further gives some evidence for the assumptions that have led to the hypotheses, which are investigated. However, the analysis is not exhaustive and only works with examplary data visualizations.

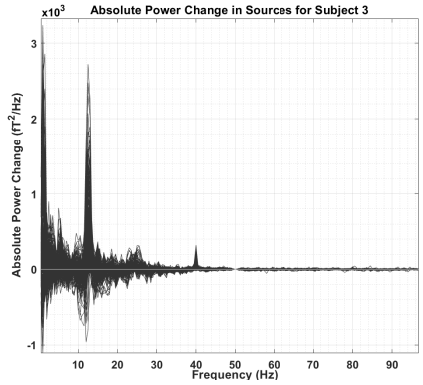

(a) Absolute Difference Spectrum.

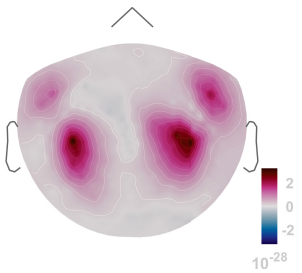

(b) Topography at 40 Hz.

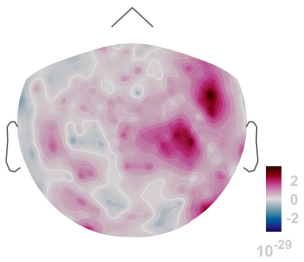

(c) Topography at 80 Hz.

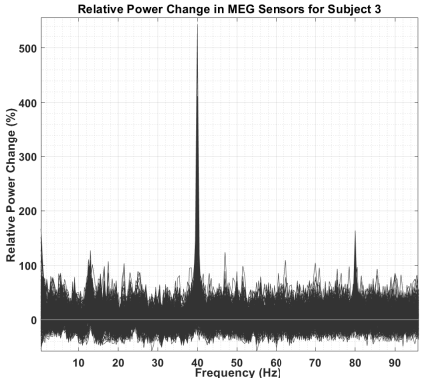

(d) Relative Difference Spectrum.

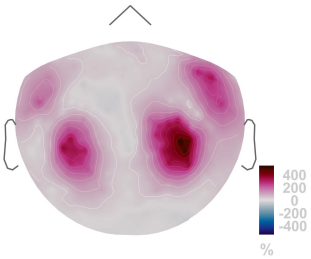

(e) Topography at 40 Hz.

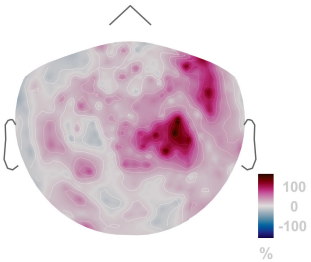

(f) Topography at 80 Hz.

Figure 4.4 Absolute (a-c) and relative (d-f) change in all MEG sensors power for subject 3 at a MF of 40 Hz. The absolute difference spectrum shows noisy behaviour for small frequencies, but also a clear peak at 40 Hz. The relative difference spectrum shows more steady noise across the different frequencies and peaks at 40 Hz and 80 Hz (harmonic response). The topographies for 40 Hz (b and e) show a clear Auditory Evoked Field with two sources, one per hemisphere. The harmonic response at 80 Hz only shows activity in the right hemisphere.

Figure 4.4 shows the absolute (4.4a) and relative (4.4d) difference spectra of all MEG sensors for a MF of 40 Hz in subject 3. As seen before in the EEG data, the noise grows for lower frequencies (especially in the alpha band) in the absolute spectrum, while it remains constant for the relative spectrum. At 40 Hz, both spectra show a peak, the relative difference spectrum also shows a smaller peak at the harmonic frequency of 80 Hz. The topographies at 40 Hz in 4.4b and 4.4e show a clear auditory evoked field with one source in each hemisphere,

which is complementary to the observed EEG topography in the previous section. A slight dominance of the signal in the right hemisphere is visible, compared to the left one. This finding is in accordance with previous studies (e.g. [40]). At 80 Hz, the topographies of both spectra show a more noisy, but still clear response of the auditory cortex in the right hemisphere. The left hemisphere however, does not show detectable activity.
An overview of the topography for other modulation frequencies and for different runs is presented in figure 4.5. For all conditions, the double dipolar topography is visible, although it does become less clear with lower frequencies in both, the relative and the absolute difference spectrum. Slight differences in the topographies over runs are possible, since the head position might change between two runs.

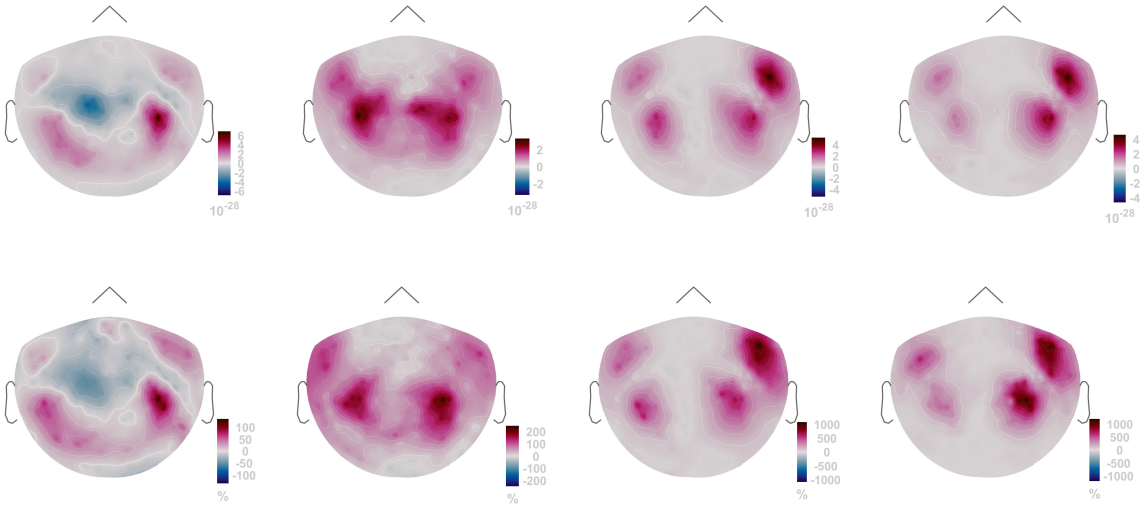

(a) 16 Hz, run 1 **(b)** 28 Hz, run 2 **(c)** 43 Hz, run 3 **(d)** 61 Hz, run 4

Figure 4.5 Topography of absolute (upper row) and relative (lower row) difference spectra for varying MFs in subject 3.

A slightly stronger activity in the right hemisphere can also be seen clearly for 16 Hz, 43 Hz and 61 Hz. For 28 Hz, both hemispheres seem identically strong. This finding confirms the assumption, that the hemispheres don't necessarily show the same behaviour in the ASSR profile.
For some MFs, the ASSR could not be found, as for example at 20 Hz in subject 3 (see figure 4.6). An enhanced activity is visible in the right frontal lobe, but the expected dipolar pattern does not differentiate from the noise. In addition, the left hemisphere seems to show only noise. This will be confirmed on the source level (see figures 4.16 and 4.18).

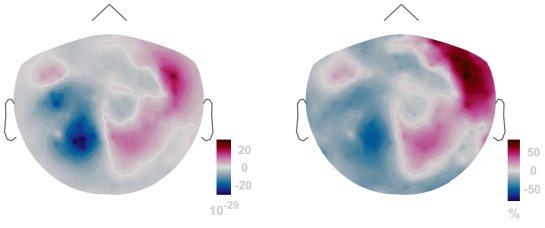

Figure 4.6 Topographies of the absolute (left) and relative (right) difference spectra at 20 Hz for a MF of 20 Hz in Subject 3.

In other subjects, the difference between the two hemispheres was a lot stronger, up to cases, in which the activity in the left hemisphere doesn't seem to exist, as illustrated in figure 4.7. On the source level in section 4.3, it will be shown, that the ASSR is also found in the left hemisphere and that it is not visible in the topography due to the large difference between the amplitudes.

For some subjects, it was impossible to gain enough information from the EEG data in order to find the ASSR (see section 4.1). However, in the MEG measurement, they did show the expected response, as can be seen exemplarily in figure 4.8. The relative difference spectrum shows a clear auditory response, while some noise can be seen in the absolute difference spectrum.

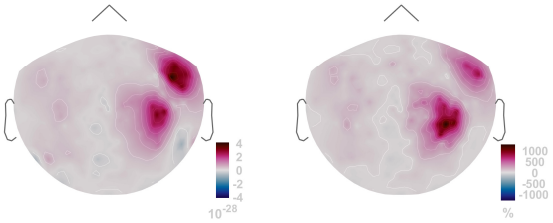

(a) Topography of the Absolute Difference Spectrum. **(b)** Topography of the Relative Difference Spectrum.

Figure 4.7 Topographies of the difference spectra at 40 Hz for a MF of 40 Hz in Subject 6. For both modalities, the right hemisphere shows the typical auditory evoked field, while no activity can be seen in the left hemisphere.

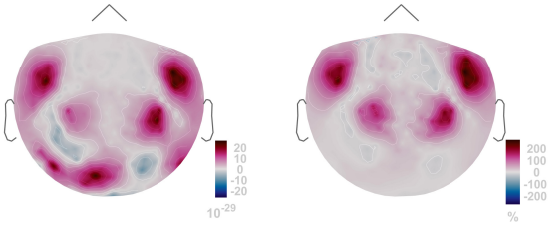

(a) Topography of the Absolute Difference Spectrum. **(b)** Topography Relative Difference Spectrum.

Figure 4.8 Topography of difference spectra at 40 Hz for a MF of 40 Hz in Subject 2. The absolute difference spectrum shows some noise, while the relative spectrum is cleaner and the dipolar pattern is visible.

4.3 MEG-Analysis on Source Level

As seen in section 4.1, the EEG-data does lead to the desired ASSR profile for most subjects. However, it is expected, that the analysis on the source level can lead to clearer results, and also to a profile that differentiates from the background for every subject. Furthermore, the source analysis offers the possibility to analyze the activity in the hemispheres individually. Hence, the sources are reconstructed from the MEG data, as described in section 3.4.5.

4.3.1 Head Model

For every subject, an individual head model was computed, consisting of the cortex and three layers: the head, the outer skull and the inner skull. An examplary head model is shown in figure 4.9. Figures 4.10a to 4.10c show the single layers and 4.10d shows the cortex. It is visible, that all surfaces are nested in the larger ones, neither touching nor crossing each other. The triangular mesh, of which the surfaces are composed, are visualized in the single layer plots.

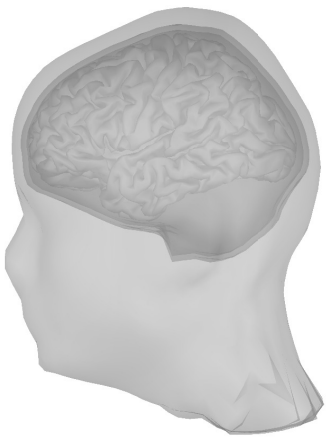

Figure 4.9 Combined layers of the BEM head model for subject 1.

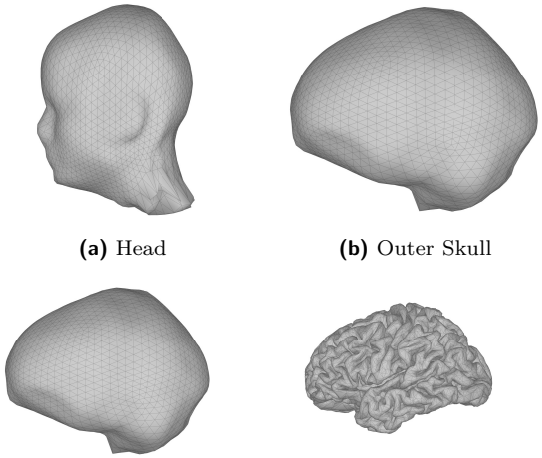

(a) Head **(b)** Outer Skull **(c)** Inner Skull **(d)** Cortex

Figure 4.10 BEM head model of subject 1: the large figure shows all relevant layers and the cortex, which serves as source space. The head, outer and inner skull and cortex also presented separately in 4.10a to 4.10d.

Based on this head geometry, the forward problem was solved for each run, resulting in one vector field for each magnetometer.

4.3.2 Source Localization

Before the source strength of the different conditions can be calculated, two regions of interest (one per hemisphere) have to be defined for every subject. Figure 4.11[12] illustrates all vertices in subject 7, which showed significantly different responses between the signal and the baseline measurement at 40 Hz. The false discovery rate criterion (FDR) was chosen as a correction method for multiple comparisons (see [5] for a detailed description). The dominance of the right hemisphere, which was also observed in the analysis of the MEG topographies, is reflected in the amount of vertices found to be significantly different and in higher corresponding t-values.

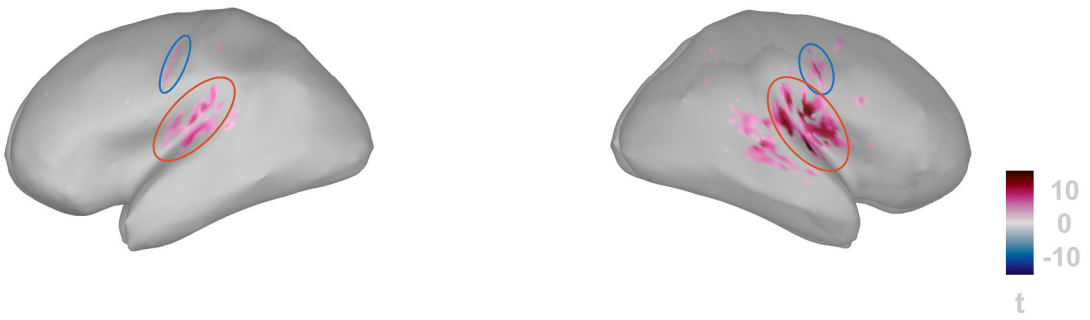

Figure 4.11 Results of the t-test in subject 7 for the left and the right hemisphere. All highlighted vertices show significant differences between the signal and the baseline ($p<0.01$), a FDR correction has been performed. The red and blue ellipses show the activity in the Heschl Gyri and the precentral Gyri respectively.

As expected, the main activity is found in the Heschl Gyri (roughly circled in red). Additionally, an activation of the precentral Gyri was observed for most subjects (roughly circled in blue). For some subjects, additional weak activity was found in other cortical regions, which disappeared by applying the amplitude threshold to extract the final region of interest (cf. section 3.4.5). Since firstly, those sources were comparatively weak and secondly, the study aims to prepare a stimulation of the auditory cortices, this rejection can be justified (see discussion for further details).
The final regions of interest, consisting of all vertices that show at least 65% of the maximum value in the corresponding hemisphere, are shown in figure 4.12. A slightly larger extended area of the right hemisphere is still visible in some subjects (e.g. subjects 1 and 6), but since the maximal values of the hemispheres were chosen independently, the difference became smaller. The extent of the chosen areas also differs between subjects. Especially subject 1 shows a relatively large region of interest. However, the analysis of the ASSR profile does not focus on the absolute strength of the sources, but on the qualitative shape and the position of

[12] For better visibility, the cortex was smoothed for the plots.

the maximum, hence the acceptance of different source extents is justified. Subject 3 shows a slightly shifted region of interest compared to the other subjects, which will be discussed in chapter 5

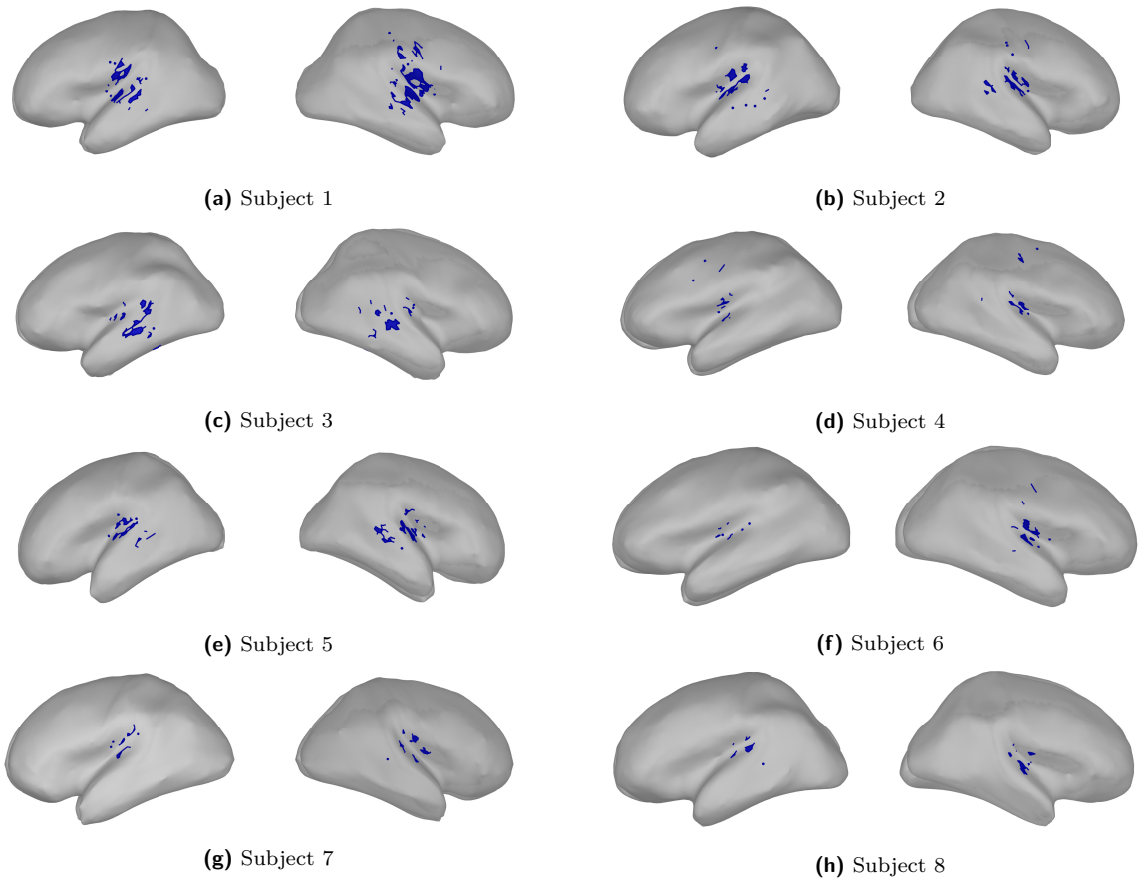

(a) Subject 1 **(b)** Subject 2

(c) Subject 3 **(d)** Subject 4

(e) Subject 5 **(f)** Subject 6

(g) Subject 7 **(h)** Subject 8

Figure 4.12 Final regions of interest in both hemispheres for all subjects.

4.3.3 ASSR profiles

In order to compute the ASSR profiles, the difference spectra have to be computed for each hemisphere and modulation frequency. Two examples of these spectra for the MF 40 Hz (figure 4.13) and 36 Hz (figure 4.14) are presented.

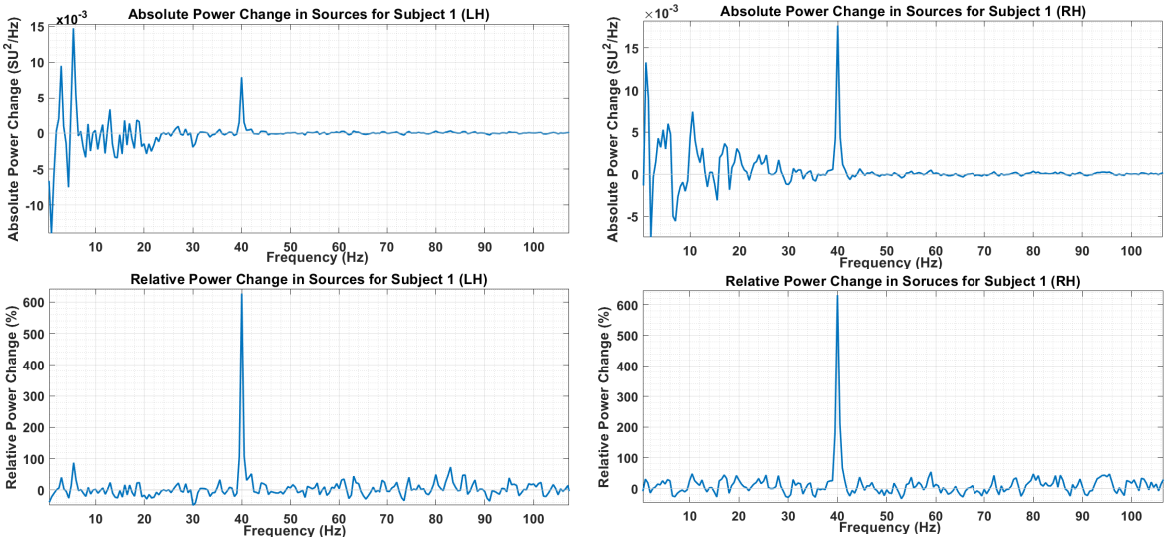

Figure 4.13 Absolute (upper row) and relative (lower row) difference spectra for the sources in the left (LH) and right (RH) hemisphere at a **MF of 40 Hz** for subject 1. All spectra show a peak at the MF. In the absolute spectra, a difference between the hemispheres is visibile, the peaks in the relative spectra show a very similar height.

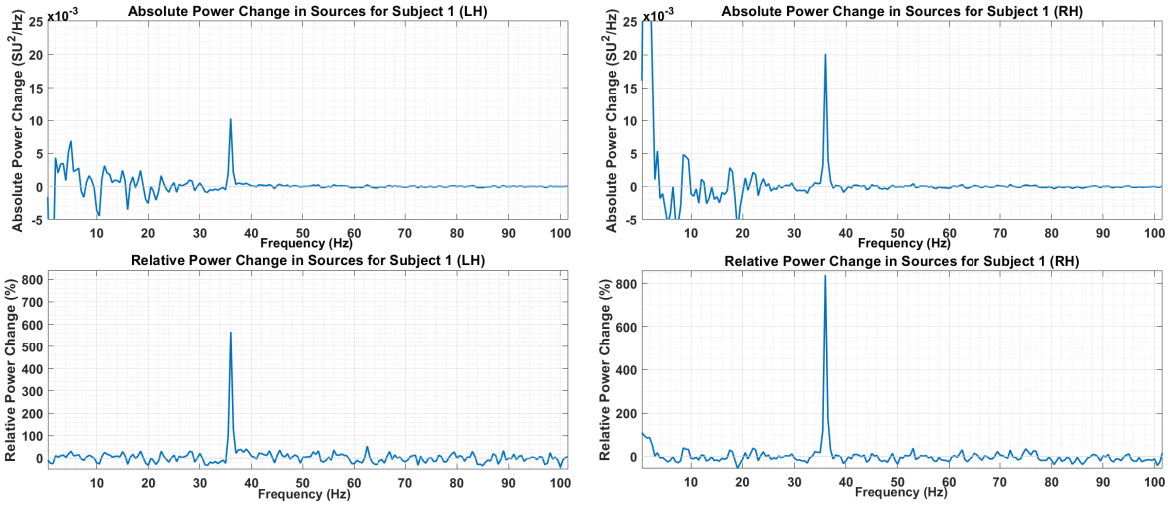

Figure 4.14 Absolute (upper row) and relative (lower row) difference spectra for the sources in the left (LH) and right (RH) hemisphere at a **MF of 36 Hz** for subject 1. All spectra show a peak at the MF. The response for the left hemisphere is weaker in both modalities.

All spectra (absolute and relative for two hemispheres) show a clear ASSR peak at 40 Hz or 36 Hz respectively. In the 40 Hz stimulation, a difference between the left and right

hemisphere is visible, with a dominance of the right hemisphere. In contrast, the relative change is approximately the same for both hemispheres. For the 36 Hz stimulation in the same subject, we find a dominance of the right hemisphere in both, the absolute and the relative difference spectra. These first results on the source level indicate, that the individual consideration of the hemispheres might indeed lead to different maxima in the ASSR profiles.

Summarizing the computed spectra for all modulation frequencies, the ASSR profiles can be created, as presented in figures 4.15 to 4.18. For all subjects in all profiles, a response that clearly stands out from the background for most modulation frequencies is visible. For some modulation frequencies however, the response can not be differentiated from the noise background and might in this case even become negative. In a first step, the qualitative behaviours of the ASSR profiles shall be presented and categorized. The exact resonance frequency will be analyzed in section 4.4.

For the absolute change in the right hemisphere (figure 4.15), the ASSR profiles of subjects 1, 2, 5 and 6 show a comparable shape with a maximum around 40 Hz with slightly increasing values for lower frequencies around 20 Hz, as it is expected from existing literature. The profile of subject 8 shows a noisy behaviour for low frequencies, but can also be put in this category. However, the other subjects show unexpected shapes of the ASSR profile. Subjects 4 and 7 show an almost monotonously decaying profile for increasing modulation frequencies, which leads to the assumption that smaller modulation frequencies might elicit even higher amplitudes. However, a small peak around 40 Hz is also visible for subject 7. The ASSR profile of subject 3 shows a high amplitude for modulation frequencies below 20 Hz and above 35 Hz, but in contrast to other subjects, it reaches a plateau at around 43 Hz.

In the left hemisphere (figure 4.16) subjects 1, 5, 6 and 8 show the same general course as in the right hemisphere. Subjects 3, which show the plateau behaviour in the right hemisphere (see above), can also be put into this category. For subject 2, the peak in low frequencies is stronger than the 40 Hz peak, hence the maximum of the ASSR profile is not found in the 40 Hz area. A similar course is observed for subject 4, in contrast to the monotonic decay in the right hemisphere. Subject 7 shows again a monotonic decay, but not as steep as in the right hemisphere.

For the relative change, the ASSR profiles of the right hemisphere show a more coherent behaviour (figure 4.17). As expected, the preference for lower frequencies has disappeared. All but two subjects show a peak around 40 Hz, which is narrower for some subjects (e.g. subjects 1 and 7) than for others (e.g. subjects 2 and 8). Subject 3, as before, approaches a plateau-like behaviour for frequencies above 40 Hz, but in contrast to the absolute ASSR profile, the peak for low frequencies has disappeared. Finally, subject 4 shows again a monotonic decay in the right hemisphere.

In the left hemisphere, all subjects show a peak around 40 Hz in the relative ASSR profile. Only in subject 4 is the maximum value still to be found in the lower frequencies.

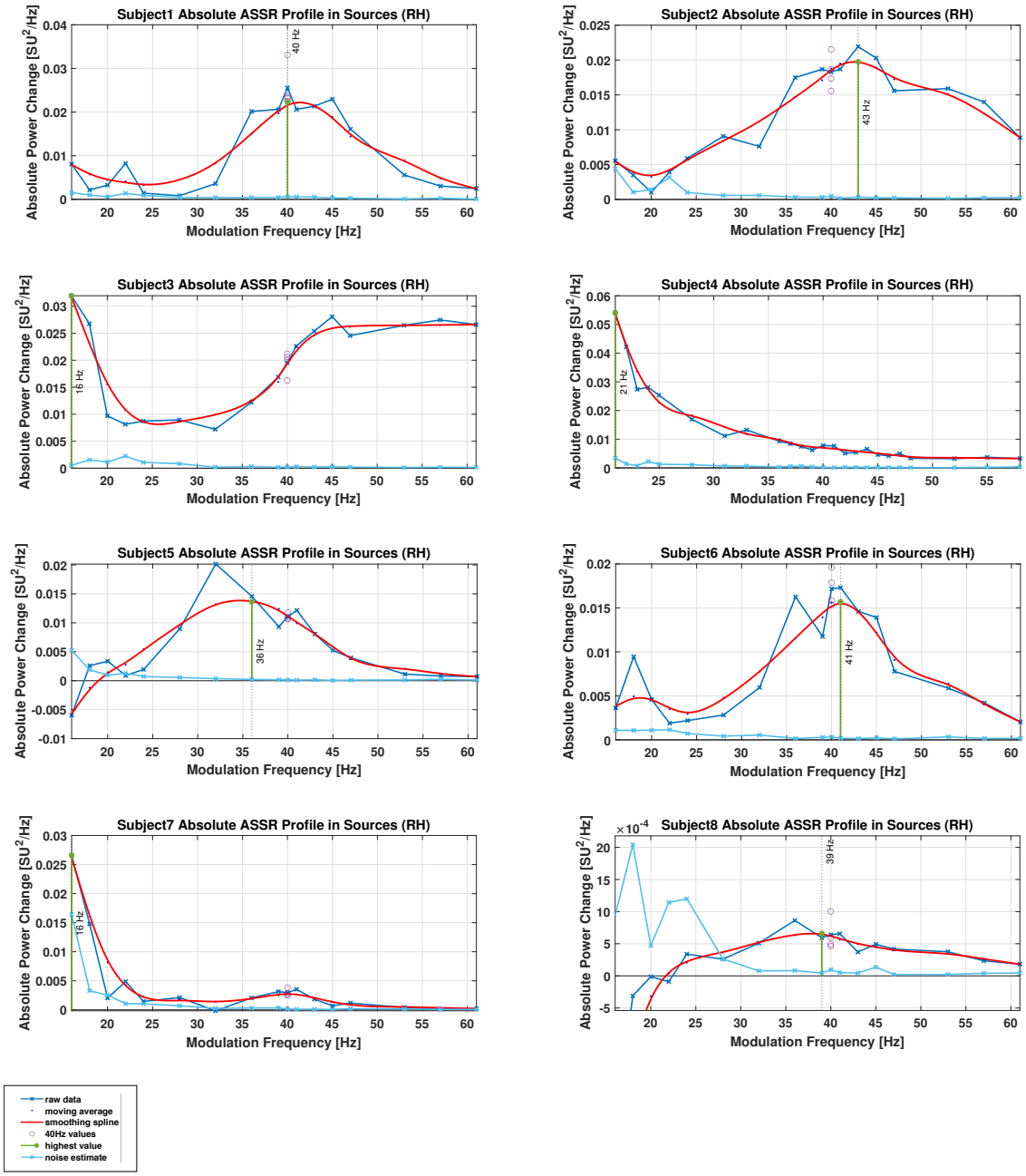

Figure 4.15 Absolute ASSR profile of the **right hemisphere** for all subjects. The raw data is marked in dark blue, the smoothed data is presented in red. An estimate of the noise is given in light blue, the maximum of the smoothed data is indicated by a green bar. Single values for 40 Hz are indicated in purple (despite subject 4). Three profile categories can be identified: Subject 1, 2, 5, 6 and 8 with a peak around 40 Hz. Subject 4, 7 with an almost monotonously decaying behaviour for higher frequencies. Subject 3 with a plateau for higher frequencies and a strongly increased amplitude for frequencies below 20 Hz.

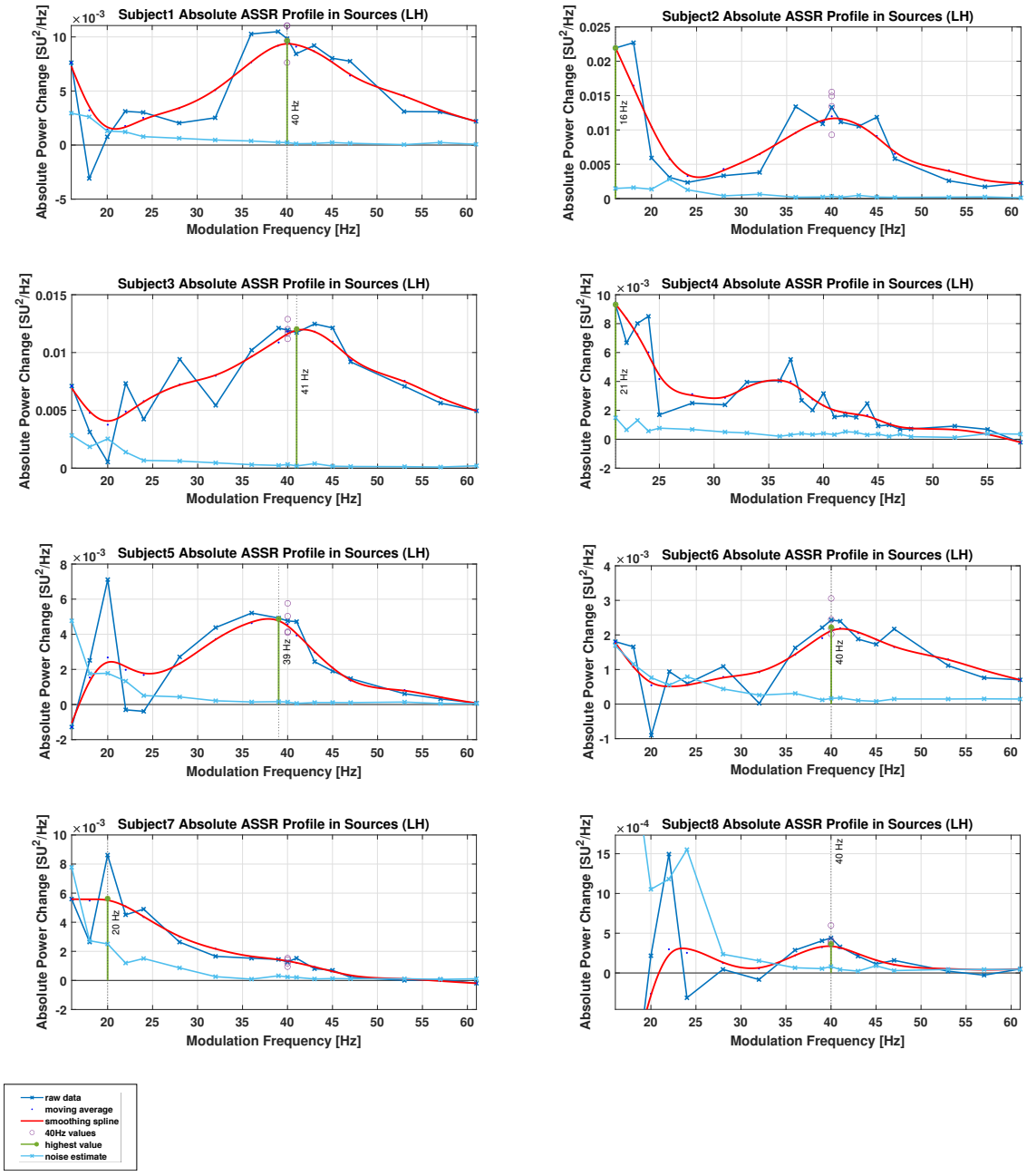

Figure 4.16 Absolute ASSR profile of the **left hemisphere** for all subjects. The raw data is marked in dark blue, the smoothed data is presented in red. An estimate of the noise is given in light blue, the maximum of the smoothed data is indicated by a green bar. Single values for 40 Hz are indicated in purple (despite subject 4). Subjects 1, 5, 6 and 8 show the same behaviour as in the right hemisphere with a peak around 40 Hz. Subject 3 can be added to this category. The monotonic decay in subject 7 is less steep, but can be identified for the left hemisphere aswell. Subjects 2 and 4 also show a peak around 40 Hz, however the maximum value is found for frequencies below 20 Hz.

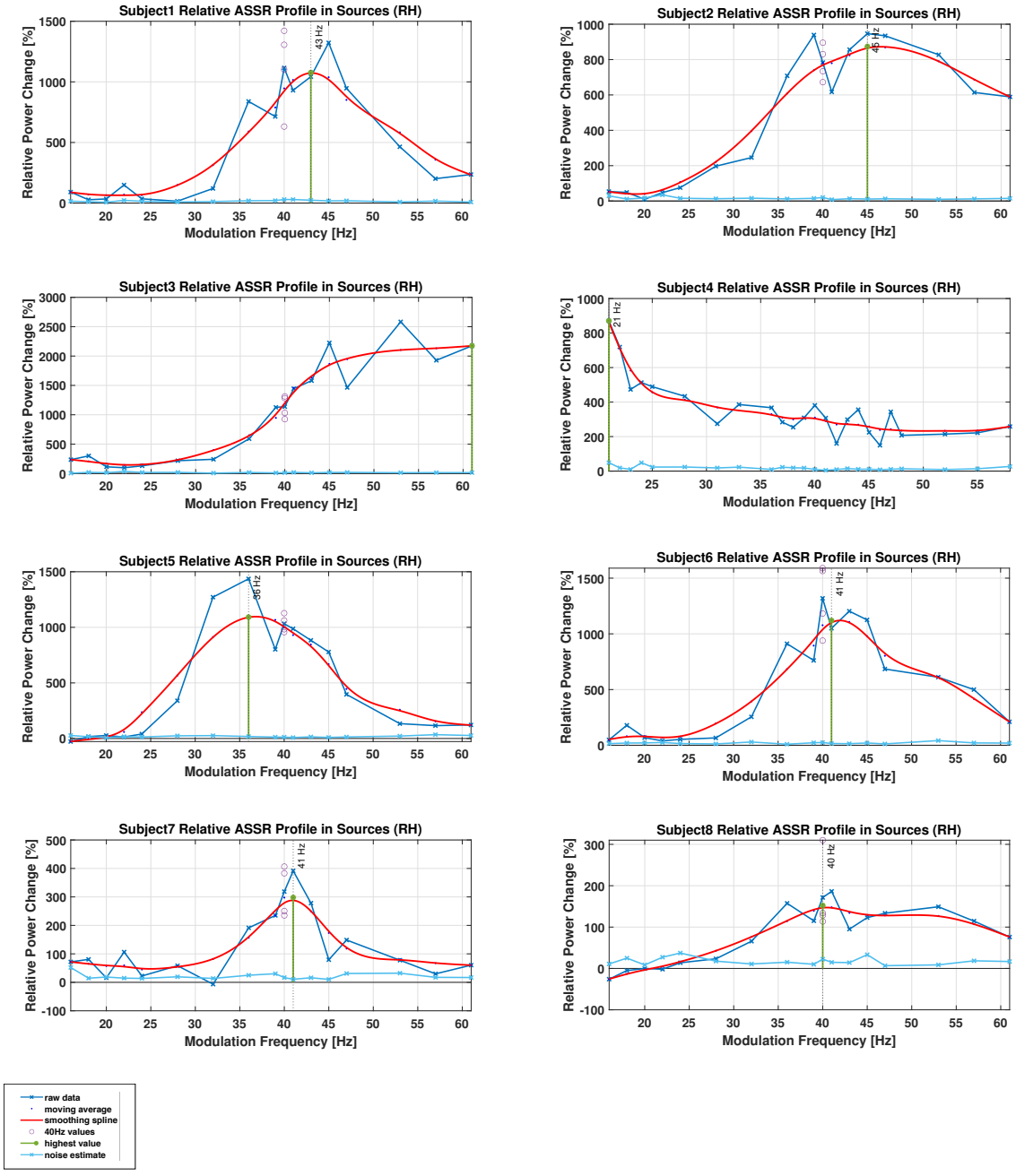

Figure 4.17 Relative ASSR profile of the **right hemisphere** for all subjects. The raw data is marked in dark blue, the smoothed data is presented in red. An estimate of the noise is given in light blue, the maximum of the smoothed data is indicated by a green bar. Single values for 40 Hz are indicated in purple (despite subject 4). Subjects 1, 2, 5, 6, 7 and 8 show a peak around 40 Hz. Subjects 3 reaches a sort plateau for frequencies above 45 Hz, subject 4 shows a monotonic decay.

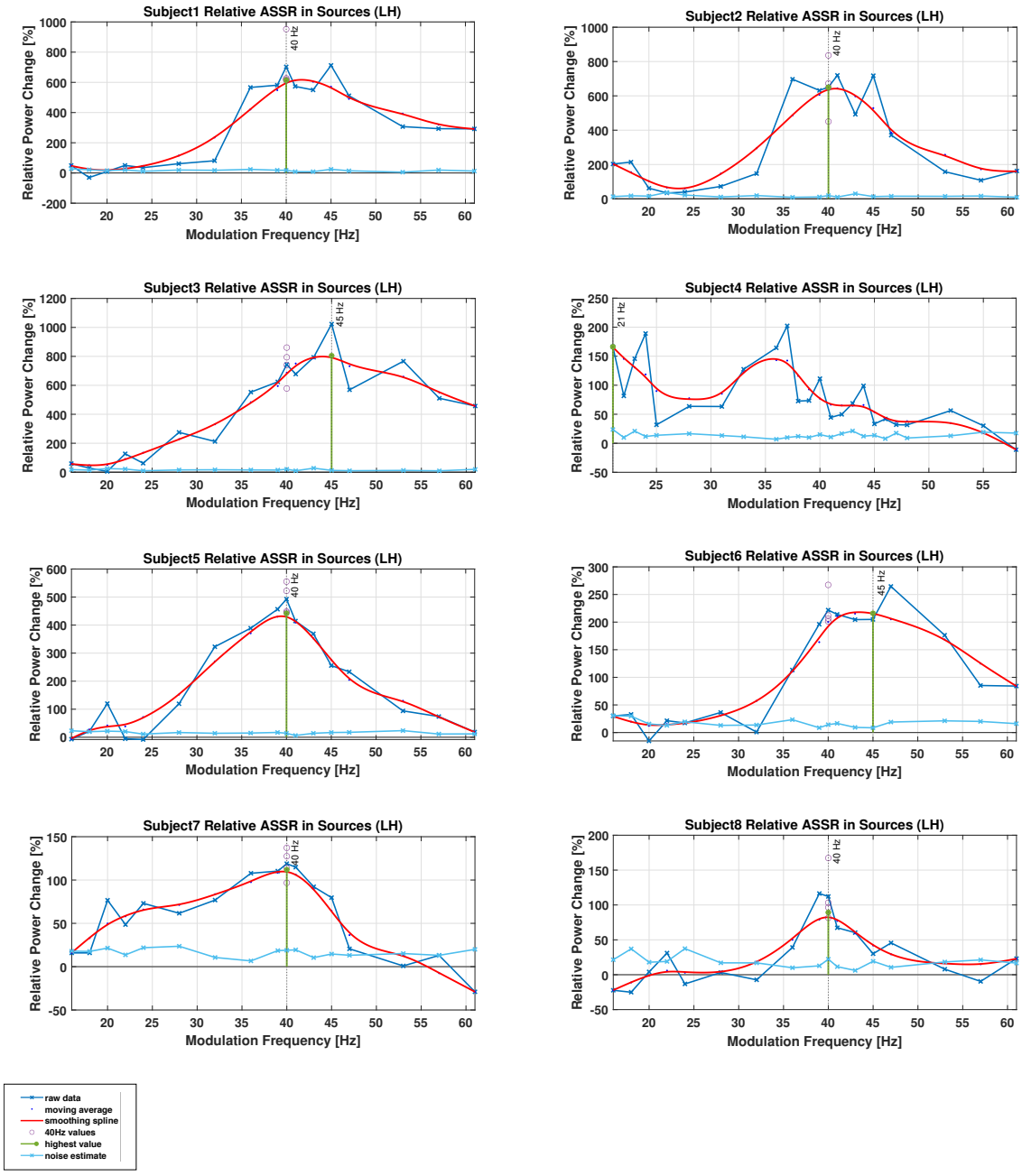

Figure 4.18 Relative ASSR profile of the **left hemisphere** for all subjects. The raw data is marked in dark blue, the smoothed data is presented in red. An estimate of the noise is given in light blue, the maximum of the smoothed data is indicated by a green bar. Single values for 40 Hz are indicated in purple (despite subject 4). All subjects show a peak around 40 Hz, which corresponds to the maximum of the profile, except subject 4, which shows the maximum in the lower frequency band.

4.4 Comparison of the Resonance Frequencies

After qualitatively analyzing the ASSR profiles, it remains to compare the resonance frequencies, which were extracted by different ways of analyzing the data. Figure 4.19 summarizes all resonance frequencies (corresponding to the green bars in the ASSR profiles). Arrows pointing to the right/left show the values determined for the right/left hemisphere. Crosses mark the value found in EEG data. For each subject, one column each is presented corresponding to the absolute and relative ASSR profile. For better visualization, the absolute columns are additionally coloured in blue, the relative columns in orange.

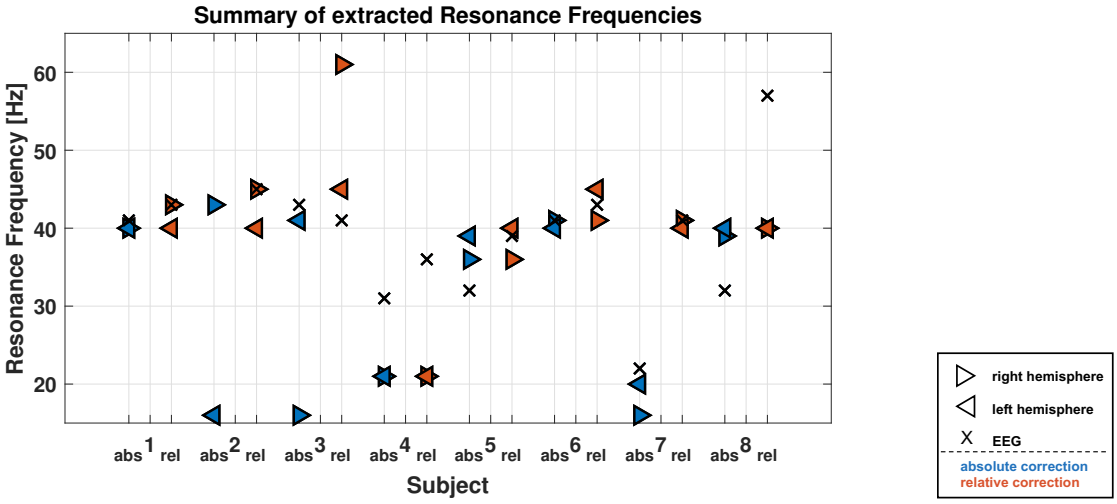

Figure 4.19 Summary of all extracted resonance frequencies. Arrows pointing to the right/left correspond to the right/left hemisphere. Blue/orange markers show values obtained by absolute/relative baseline correction. Crosses show the value obtained by EEG sensor data.

Most resonance frequencies are found to be in the range from 36 Hz to 45 Hz. An exact match between the two hemispheres is found in only four cases (subject 1 absolute, subject 4 absolute and relative, subject 8 relative). In general, a small difference between the maximal values of both hemispheres can be observed. For the absolute baseline correction, the mean difference between the hemispheres is 7.6 Hz (SD: 11.4 Hz), ranging from 0 Hz to 27 Hz, for the relative correction 4.1 Hz (SD: 5.2 Hz), ranging from 0 Hz to 16 Hz. Table 2 shows the resulting differences for all subjects. Subjects 2 and 3 show the largest difference between the hemispheres (Subject 3 for relative and absolute correction, subject 2 only for absolute correction). The differences between the resonance frequencies found in EEG and each hemisphere were also computed. While the determined resonance frequencies of the EEG resonance frequency deviate 7.8 Hz (SD: 9.1 Hz) for the absolute correction and 8.1 Hz (SD: 8.8 Hz) for the relative correction from the right hemisphere, the difference to left hemisphere is 4.4 Hz (SD: 3.8 Hz) and 6.1Hz (SD: 6.8 Hz) respectively. Hence, for this small sample, the resonance frequency determined by EEG is in average closer to the left hemisphere than to the right hemisphere. When evaluating the individual values however, neither hemisphere

corresponds clearly to the resonance frequency detected by EEG.

Table 2 Extracted Resonance Frequencies for EEG and both hemispheres using absolute and relative baseline correction in Hertz. Values in brackets can't be distinguished from the background and excluded from further analysis.

	EEG		**RH**		**LH**		**|EEG-RH|**		**|EEG-LH|**		**|RH-LH|**	
	abs	rel	abs	rel	abs	rel	abs	rel	abs	rel	abs	rel
S1	41	43	40	43	40	40	1	0	1	3	0	3
S2	[22]	[45]	43	45	16	40	NaN	NaN	NaN	NaN	27	5
S3	43	41	16	61	41	45	27	20	2	4	25	16
S4	31	36	21	21	21	21	10	15	10	15	0	0
S5	32	39	36	36	39	40	4	3	7	1	3	4
S6	41	43	41	41	40	45	0	2	1	2	1	4
S7	22	41	16	41	20	40	6	0	2	1	4	1
S8	32	57	39	40	40	40	7	17	8	17	1	0
M							7.9	8.1	4.4	6.1	7.6	4.1
SD							9.1	8.8	3.8	6.8	11.4	5.2

5 Discussion

The main goal was to evaluate, whether the resonance frequency detected by a single central electrode analysis is in accordance with the one obtained by an MEG source analysis. Since the two hemispheres are expected to provide different resonance frequencies, it is expected, that the EEG data is dominated by the stronger hemisphere (i.e. the right hemisphere).
For all MEG sources, a sufficient ASSR profile could be extracted for the analysis. The study however is limited by the quality of the EEG data, since it turned out to be rather noisy and therefore not all subjects could be properly analyzed on the EEG level. The reasons for this are twofold: On the one hand, all data was collected in one session in order to minimize the recording time. As a large modulation frequency range was scanned, only limited data per condition was available. On the other hand, by the time of the data recordings, the institute was waiting for the commissioning of a new EEG device, since the one that was eventually used, was known to produce comparatively much noise. Nevertheless, after data cleansing, the data quality of most subjects sufficed to be compared to the MEG source data. It is however suggested to extend the study by further subjects once the new EEG device is available. The explorative results presented in this study point to new research questions, which should be investigated in further studies, as will be discussed in this chapter.

Source Localization

The activities in the Heschl Gyri and the precentral Gyri found in section 4.3.2 are in concordance with the ones found in [15]. The additional weak activity, which was neglected, is likely to result from activity in subcortical regions (i.e. brainstem and thalamus), which is known to occur in the ASSR. The difference in the source extent is likely to result from the cut-off point for the amplitude, which was defined in a way to show reasonable results for all subjects, but still chosen arbitrarily. If the maximum is very high compared to the remaining activity (for example an outlier), more vertices are excluded by the threshold than for a maximum, which shows a similar strength as the remaining activity. Nevertheless, this different extent is not expected to change the results, as the absolute strength is not interpreted in this study and only the average source strength in all vertices of the region of interest is considered. Other definitions of the region of interest are conceivable, such as the limitation by a projected atlas or by a maximal spatial extent, but these procedures require more pre-assumptions concerning the source location and were therefore avoided.
Subject 3 shows a main activity slightly shifted from the Heschl Gyrus in both hemispheres. So far, no cause for this deviation could be identified and therefore the results were kept and the deviation will be considered in the further discussion of the results. Despite utmost care on the part of the author, an error in the recordings or the registration of the different modalities cannot be ruled out completely and the interpretation of these results is therefore treated with care.

ASSR Profiles

The analysis revealed, that differences in the qualitative shape of the ASSR profiles can be found between subjects, but also between hemispheres. The latter finding is consistent with the existing literature in a way, that the hemispheres react differently on changes in the stimulus, as was investigated in [31]. The laterality at 40 Hz was found to be right for all subjects, in accordance with Ross et al. [34] rather than Yamasaki et al. [48].
The results imply, that there are different types of ASSR profile shapes. The most prominent type in this sample is the one often discussed in the literature with a peak around 40 Hz and slightly increasing activity for low frequencies in the case of absolute baseline correction. However, in some cases the amplitudes for low modulation frequencies increase in a way, that they exceed the 40 Hz peak. In extreme cases, the 40 Hz is barely visible (subject 7, RH, absolute) or even non-detectable (subject 4, RH, absolute and relative), resulting in the second type, which shows an (almost) monotonic decrease of the amplitude for increasing modulation frequencies. Subject 3 showed a plateau-like behaviour, which was identified as a third type. However, since this ASSR profile shape was not oberserved in any other subjects, it is possible, that this unique behaviour is associated with the shifted source localization discussed above.
The distinction between ASSR profile types was also made by Baltus et al. [2]. In this study, subjects, whose ASSR profiles did not show a local maximum, were excluded from further analysis. Since this affected no less than 11 out of 46 subjects, further investigation on other ASSR profiles is suggested.

Resonance Frequencies

The main interest of this study was a comparison of the resonance frequency obtained by EEG sensor analysis and the ones in each hemisphere obtained by MEG source reconstruction. The analysis in section 4.4 has shown, that in most subjects differences were found between all three extracted resonance frequencies for both ways of baseline correction. The averaged results imply, that the resonance frequency found by EEG is closer to the one found for the left hemisphere than to the one found for the right hemisphere (see table 2), which would be the contrary of what was expected. However, on an individual level, this finding is not confirmed and EEG is not generally in higher concordance with either hemisphere. Although it was expected, that the right hemisphere dominates the values found in EEG, only some conditions showed this behaviour. An exact match was only found in few subjects and half of the subjects showed a closer relation between EEG and the left hemisphere. Therefore, no final statement can be made about which hemisphere dominates the central EEG recordings. One cause of this observed phenomenon might be, that the hemispheres dominate for different modulation frequencies, if the asymmetry between the hemispheres is not too strong. Since

the computation of the laterality requires the absolute source strengths, the data has to be re-evalutated in a different manner to test this hypothesis. Nevertheless, the MEG-sensor data presented in figure 4.5 implies, that the laterality does indeed change with the modulation frequency and it seems possible to have a domination of the left hemisphere for certain modulation frequencies. Another factor might be the source orientation, which has been neglected in this study. If the orientations in the hemispheres are not symmetrical or change for varying modulation frequencies, the components seen by MEG or EEG might differ. Further investigation on the source orientation in each hemisphere for different modulation frequencies is therefore suggested.
Consequently, it is not possible to get a holistic picture of the activities in the auditory cortices by a single or few central EEG-electrode analysis, since the activities of both sources fuse in the frontal central lobe. Measurements should be conducted by non-central electrodes as in [31] or preferably with MEG, since it shows the activity more clearly.

The results further imply, that for an optimal stimulation of the brain with alternating currents, a separate targeting of the auditory cortices with different frequencies is needed in some subjects, if the stimulation is to occur at a modulation frequency which slightly exceeds the resonance frequency. In previous studies, a choice of 4 Hz above the resonance frequency was chosen based on findings in [2]. Since this frequency is very close to the resonance frequency, even small inter-hemispheric differences as found in most of the subjects would lead to a suboptimal stimulation. A study by Poelmans et al. [30] has further shown, that the ASSR strength in the left hemisphere is reduced for modulation frequencies near 20 Hz in a group suffering from dyslexia. The interhemispheric difference of the resonance frequencies is therefore expected to be even stronger in such subjects and since they are a possible target group for tACS, an asymmetric stimulation seems especially interesting.
It is noted, that in some cases, the resonance frequency was determined at the lowest modulation frequency under investigation. This result seems insufficient, since the profile indicated even higher amplitudes for lower modulation frequencies. The findings therefore suggest, that it might be useful to first measure a rough version of the ASSR profile, before then densely scanning the frequency regions of interest. However, this procedure is more time consuming and might not be applicable in all studies.

Baseline correction methods

With regard to baseline correction methods, the relative correction leads to a cleaner and more coherent picture between subjects and between hemispheres than the absolute one. However, it is a matter of discussion which modality should be founding the determination of the resonance frequency. The relative correction showed a weaker activity change in the lower frequencies than the absolute correction method. This finding can be explained with the 1/f behaviour: for lower frequencies a stronger baseline activity is found. Hence the

relative change of the amplitude is weaker for lower frequencies. Both methods are well established and therefore more insight on the phenomenon of the resonance frequency is needed in order to decide, which method should be chosen. The fundamental question that needs to be answered is, which frequency has to be stimulated in order to obtain the highest effect. Therefore, a study is suggested, which investigates the effect size, when stimulating with the absolute or relative resonance frequencies (or slightly above these resp.). If a preference for one of the methods is found, this one should be picked for stimulation. Further, this result would give more insight about the nature of the power spectrum and would also be relevant for numerous other research areas.
In previous studies (e.g. [2, 49]), yet another correction method has been utilized, namely the multiplication of the spectral values by their frequency. The underlying idea is to correct for the 1/f behaviour. Strictly spoken, this procedure does not describe a baseline correction, but rather a standardization method, which should not be used for further analysis, but only for visualization purposes. If applying this multiplication, the effect (i.e. the peak in the spectrum) is weighted by the modulation frequency, resulting in a distorted comparison between the different conditions.

Brainstorm

The toolbox Brainstorm has been found to be a strong tool in the analysis. The usage is intuitive and the integration into Matlab makes it easy to create scripts, the combination of a graphical user interface and the possibility to include own scripts has been found to make the analysis both, vivid and efficient. All steps in the analysis were successfully conducted without any other software (except Matlab). The Brainstorm community offers a forum, in which bugs in the code and content or technical questions can be asked or discussed and it has proven to be very helpful. Brainstorm is always working on integrating new or improved methods into their pipelines. Therefore, the available options in Brainstorm grow permanently and will offer even more analysis options in the future. One example is the duneuro FEM-modeling [37], which is currently being integrated. Unfortunately, a combined source analysis of EEG and MEG data is not yet implemented and only leaves the option of two separate analyses, which can be compared. Furthermore, the options when it comes to fitting a dipole are limited. However, overall the further utilization of Brainstorm is recommended by the author.

6 Conclusion

ASSR profiles and the resulting resonance frequencies have succesfully been extracted for different modalities. The shapes of the profiles were categorized and at least two qualitatively different types were identified. The study has shown, that the hemispheres of the same subjects show different resonance frequencies. No consistency in the direction of the difference has been found yet and needs further investigation. However, the results imply, that tACS should be performed with different frequencies in both hemispheres in order to maximize the effect size. In addition, the difference between the hemispheres causes a wrong resonance frequency estimate in the central EEG electrodes, which might result from a change in laterality or source orientation for varying modulation frequencies. It is therefore recommended to determine the resonance frequency with MEG or with non-central electrodes as in [31].

It was further shown, that the choice of the baseline correction method influences the resulting resonance frequencies. The absolute and the relative change in activity was compared. Due to the aperiodic background, the relative correction favors the higher frequencies and the absolute correction favors the lower frequencies. Overall, the relative correction showed a better SNR, which might be an indicator for the preference of this method. Furthermore, the ASSR profiles obtained by the relative correction showed a more coherent shape between subjects and hemispheres. It should nevertheless be evaluated, which resonance frequency leads to a higher effect in the brain stimulation, since it could provide information about the nature of the power spectrum. Limits of this study were a relatively small sample size and comparatively much noise in the EEG data.

The toolbox Brainstorm has been successfully used to perform the entire data analysis without further software and is therefore recommended for further utilization.

References

[1] G. B. Azzena, G. Conti, R. Santarelli, F. Ottaviani, G. Paludetti, and M. Maurizi. Generation of human auditory steadystate responses (SSRs). i: Stimulus rate effects. *Hearing Research*, 83(1):1–8, 1995.

[2] A. Baltus and C. S. Herrmann. Auditory temporal resolution is linked to resonance frequency of the auditory cortex. *International Journal of Psychophysiology*, 98(1):1–7, 2015.

[3] A. Baltus, S. Wagner, C. H. Wolters, and C. S. Herrmann. Optimized auditory transcranial alternating current stimulation improves individual auditory temporal resolution. *Brain Stimulation*, 11(1):118–124, 2018.

[4] E. Başar, B. Rosen, C. Başar-Eroglu, and F. Greitschus. The associations between 40 Hz-EEG and the middle latency response of the auditory evoked potential. *International Journal of Neuroscience*, 33(1-2):103–117, 01 1987.

[5] Y. Benjamini and Y. Hochberg. Controlling the false discovery rate: A practical and powerful approach to multiple testing. *Journal of the Royal Statistical Society: Series B (Methodological)*, 57(1):289–300, 1995.

[6] H. Berger. Über das Elektrenkephalogramm des Menschen. *Archiv für Psychiatrie und Nervenkrankheiten*, 87:527–570, 1929.

[7] D. H. Brainard. The Psychophysics Toolbox. *Spatial Vision*, 10(4):433 – 436, 01 Jan. 1997.

[8] N. Campbell and J. Reece. *Biologie*, volume 8. Pearson Studium, 2009.

[9] D. Cohen. Magnetoencephalography: Evidence of Magnetic Fields Produced by Alpha-Rhythm Currents. *Science*, 161(3843):784–786, 1968.

[10] A. M. Dale, A. K. Liu, B. R. Fischl, R. L. Buckner, J. W. Belliveau, J. D. Lewine, and E. Halgren. Dynamic statistical parametric mapping: Combining fMRI and MEG for high-resolution imaging of cortical activity. *Neuron*, 26(1):55–67, 2000.

[11] A. M. Dale and M. I. Sereno. Improved localization of cortical activity by combining EEG and MEG with MRI cortical surface reconstruction: A linear approach. *Journal of cognitive neuroscience*, 5(2):162–176, 1993.

[12] J. C. de Munck, C. H. Wolters, and M. Clerc. EEG and MEG: forward modeling. In R. Brette and A. Destexhe, editors, *Handbook of Neural Activity Measurement*. Cambridge University Press, 2012.

[13] R. Dean Linden, T. W. Picton, G. Hamel, and K. B. Campbell. Human auditory steady-state evoked potentials during selective attention. *Electroencephalography and Clinical Neurophysiology*, 66(2):145–159, 1987.

[14] T. Donoghue, M. Haller, E. J. Peterson, P. Varma, P. Sebastian, R. Gao, T. Noto, A. H. Lara, J. D. Wallis, R. T. Knight, A. Shestyuk, and B. Voytek. Parameterizing neural power spectra into periodic and aperiodic components. *Nature Neuroscience*, 23(12):1655–1665, 2020.

[15] E. D. Farahani, J. Wouters, and A. van Wieringen. Improving source modeling of auditory steady-state responses with frequency-specific brain maps. *bioRxiv*, 2019.

[16] R. Galambos, S. Makeig, and P. J. Talmachoff. A 40-Hz auditory potential recorded from the human scalp. *Proceedings of the National Academy of Sciences of the United States of America*, 78(4):2643–2647, 04 1981.

[17] C. Gaser and R. Dahnke. CAT-a computational anatomy toolbox for the analysis of structural MRI data. *Hgm*, 2016:336–348, 2016.

[18] A. Gramfort, T. Papadopoulo, E. Olivi, and M. Clerc. OpenMEEG: opensource software for quasistatic bioelectromagnetics. *BioMedical Engineering OnLine*, 9(1):45, 2010.

[19] J. A. Hämäläinen, A. Rupp, F. Soltész, D. Szücs, and U. Goswami. Reduced phase locking to slow amplitude modulation in adults with dyslexia: An MEG study. *NeuroImage*, 59(3):2952–2961, 2012.

[20] M. Hämäläinen, R. Hari, R. J. Ilmoniemi, J. Knuutila, and O. V. Lounasmaa. Magnetoencephalography—theory, instrumentation, and applications to noninvasive studies of the working human brain. *Rev. Mod. Phys.*, 65:413–497, Apr 1993.

[21] M. S. Hämäläinen and R. J. Ilmoniemi. Interpreting magnetic fields of the brain: minimum norm estimates. *Medical & Biological Engineering & Computing*, 32(1):35–42, 1994.

[22] R. Hari, S. Baillet, G. Barnes, R. Burgess, N. Forss, J. Gross, M. Hämäläinen, O. Jensen, R. Kakigi, F. Mauguière, N. Nakasato, A. Puce, G.-L. Romani, A. Schnitzler, and S. Taulu. IFCN-endorsed practical guidelines for clinical magnetoencephalography (MEG). *Clinical Neurophysiology*, 129(8):1720 – 1747, 2018.

[23] R. Hari, M. Hämäläinen, and S. Joutsiniemi. Neuromagnetic steady-state responses to auditory stimuli. *The Journal of the Acoustical Society of America*, 86(3):1033–1039, 2020/02/19 1989.

[24] P. Korczak, J. Smart, R. Delgado, T. Strobel, and C. Bradford. Auditory steady-state responses. *Journal of the American Academy of Audiology*, 23:146–70, 03 2012.

[25] J. Kybic, M. Clerc, T. Abboud, O. Faugeras, R. Keriven, and T. Papadopoulo. A common formalism for the integral formulations of the forward eeg problem. *IEEE Transactions on Medical Imaging*, 24(1):12–28, Jan 2005.

[26] K. T. Legget, A. K. Hild, S. E. Steinmetz, S. T. Simon, and D. C. Rojas. MEG and EEG demonstrate similar test-retest reliability of the 40Hz auditory steady-state response. *International journal of psychophysiology : official journal of the International Organization of Psychophysiology*, 114:16–23, 04 2017.

[27] C. Pantev, L. Roberts, T. Elbert, B. Roß, and C. Wienbruch. Tonotopic organization of the sources of human auditory steady-state responses. *Hearing Research*, 101(1):62–74, 1996.

[28] T. W. Picton. *Human Auditory Evoked Potentials.* Plural Publishing, Inc., San Diego, UNITED STATES, 2010.

[29] G. Plourde, D. R. Stapells, and T. W. Picton. The human auditory steady-state evoked potentials. *Acta Oto-Laryngologica*, 111(sup491):153–160, 01 1991.

[30] H. Poelmans, H. Luts, M. Vandermosten, B. Boets, P. Ghesquière, and J. Wouters. Auditory steady state cortical responses indicate deviant phonemic-rate processing in adults with dyslexia. *Ear and hearing*, 33(1):134–143, 2012.

[31] H. Poelmans, H. Luts, M. Vandermosten, P. Ghesquière, and J. Wouters. Hemispheric asymmetry of auditory steady-state responses to monaural and diotic stimulation. *Journal of the Association for Research in Otolaryngology*, 13(6):867–876, 2012.

[32] T. Popov, R. Oostenveld, and J. M. Schoffelen. FieldTrip made easy: An analysis protocol for group analysis of the auditory steady state brain response in time, frequency, and space. *Frontiers in Neuroscience*, 12:711, 2018.

[33] B. Ross, C. Borgmann, R. Draganova, L. E. Roberts, and C. Pantev. A high-precision magnetoencephalographic study of human auditory steady-state responses to amplitude-modulated tones. *The Journal of the Acoustical Society of America*, 108(2):679–691, 2000.

[34] B. Ross, A. Herdman, and C. Pantev. Right Hemispheric Laterality of Human 40 Hz Auditory Steady-state Responses. *Cerebral Cortex*, 15(12):2029–2039, 03 2005.

[35] B. Ross, T. Picton, A. Herdman, and C. Pantev. The effect of attention on the auditory steady-state response. *Neurology and clinical neurophysiology : NCN*, 2004:22, 2004.

[36] R. Santarelli, M. Maurizi, G. Conti, F. Ottaviani, G. Paludetti, and V. E. Pettorossi. Generation of human auditory steady-state responses (SSRs). II: Addition of responses to individual stimuli. *Hearing Research*, 83(1):9–18, 1995.

[37] S. Schrader, A. Westhoff, M. Carla Piastra, T. Miinalainen, S. Pursiainen, J. Vorwerk, H. Brinck, C. H. Wolters, and C. Engwer. DUNEuro – A software toolbox for forward modeling in bioelectromagnetism. *arXiv e-prints*, page arXiv:1901.02874, Jan. 2019.

[38] D. R. Stapells, R. Galambos, J. A. Costello, and S. Makeig. Inconsistency of auditory middle latency and steady-state responses in infants. *Electroencephalography and Clinical Neurophysiology/Evoked Potentials Section*, 71(4):289–295, 1988.

[39] F. Tadel, S. Baillet, J. C. Mosher, D. Pantazis, and R. M. Leahy. Brainstorm: A User-Friendly Application for MEG/EEG Analysis. *Computational Intelligence and Neuroscience*, 2011:879716, 2011.

[40] H. R. M. Tan, J. Gross, and P. J. Uhlhaas. MEG—measured auditory steady-state oscillations show high test–retest reliability: A sensor and source-space analysis. *NeuroImage*, 122:417–426, 2015.

[41] X. Tan, Q. Fu, H. Yuan, L. Ding, and T. Wang. Improved Transient Response Estimations in Predicting 40 Hz Auditory Steady-State Response Using Deconvolution Methods. *Frontiers in Neuroscience*, 11:697, 2017.

[42] W. Tatum. Normal EEG. In W. Tatum, editor, *Handbook of EEG Interpretation*. Demos Medical Publishing, 2014.

[43] H. Thuné, M. Recasens, and P. J. Uhlhaas. The 40-hz auditory steady-state response in patients with schizophrenia: A meta-analysis. *JAMA Psychiatry*, 73(11):1145–1153, 2/19/2020 2016.

[44] Universitätsklinikum Giessen und Marburg. Magnetresonanz-Tomographie. Lernskript für Mediziner, January 2013.

[45] S. Vanvooren, H. Poelmans, M. Hofmann, P. Ghesquière, and J. Wouters. Hemispheric asymmetry in auditory processing of speech envelope modulations in prereading children. *Journal of Neuroscience*, 34(4):1523–1529, 2014.

[46] D. Weishaupt, V. D. Köchli, and B. Marincez. *Wie funktioniert MRI? Eine Einführung in Physik und Funktionsweise der Magnetresonanzbildgebung*, volume 7. Springer, 2014.

[47] P. Welch. The use of fast fourier transform for the estimation of power spectra: A method based on time averaging over short, modified periodograms. *IEEE Transactions on Audio and Electroacoustics*, 15(2):70–73, June 1967.

[48] T. Yamasaki, Y. Goto, T. Taniwaki, N. Kinukawa, J.-i. Kira, and S. Tobimatsu. Left hemisphere specialization for rapid temporal processing: a study with auditory 40Hz steady-state responses. *Clinical Neurophysiology*, 116(2):393–400, 2005.

[49] T. Zaehle, D. Lenz, F. W. Ohl, and C. S. Herrmann. Resonance phenomena in the human auditory cortex: individual resonance frequencies of the cerebral cortex determine electrophysiological responses. *Experimental Brain Research*, 203(3):629–635, 2010.

Plagiatserklärung

Hiermit versichere ich, Yvonne Buschermöhle, dass ich die vorliegende Arbeit "Source Analysis of the Auditory Steady State Response for varying Modulation Frequencies: A combined EEG-MEG Group Study" selbstständig verfasst und keine anderen als die angegebenen Quellen und Hilfsmittel benutzt habe. Die Stellen der Arbeit, die ich anderen Werken dem Wortlaut oder dem Sinn nach entnommen habe, wurden in jedem Fall unter Angabe der Quellen der Entlehnung kenntlich gemacht. Das Gleiche gilt auch für Tabellen, Skizzen, Zeichnungen, bildliche Darstellungen usw. Die Masterarbeit habe ich nicht, auch nicht auszugsweise, für eine andere abgeschlossene Prüfung angefertigt.

Ort, Datum Yvonne Buschermöhle

Ich erkläre mich mit einem Abgleich der Arbeit mit anderen Texten zwecks Auffindung von Übereinstimmungen sowie mit einer zu diesem Zweck vorzunehmenden Speicherung der Arbeit in eine Datenbank einverstanden.

Ort, Datum Yvonne Buschermöhle